"deflect" sunlight to the ground; thus surface points that already receive direct sunlight through (often substantial) gaps in the cloud field receive an added amount of light. Without careful 3D radiative modeling of this effect —and this is *not* in our present operational capabilities— we will infer spurious values of ground reflectance, hence surface properties. A standard cloud mask describes obstruction of *viewing* by cloud and can warn about —but if not cure– potential problems in the quantitative interpretation of day-time MTI scenes. A non-standard counterpart for *insolation*, or "cloud-shadow" mask, would also be helpful but remains, for the moment, an research project.

For night-time observations, the situation is fortunately less complex in the thermal IR, due to the quasi-absence of multiple scatterings and/or surface reflections. In the limit of no atmospheric scattering whatsoever, radiative transfer is tractable, at least numerically, in the arbitrarily geometry. We are therefore in a better position to control/quantify the effect of assumptions such as using a single temperature to describe the whole atmosphere. Here the cloud mask is still important but, in final analysis, a larger portion of a cloud-contaminated scene is likely to be usable.

11.2 Scientific Basis

11. 2. 1 Context

At this point, we need to summarize the status of cloud radiative transfer theory in the solar spectrum *from the operational perspective.*

It is fair to say that ...

> pending the outcome of the current "cloud absorption anomaly" debate [Cess *et al.*, 1996; Imre *et al.*, 1996; and references therein], the jury is still out on the applicability of standard (homogenous plane-parallel) models for predicting cloud radiative properties *at scales of interest to climate studies* as required, e.g., in GCM radiation parameterizations.

The reason such simplistic models of cloud structure are viable at all is traceable to cancellation at large-enough scales [Marshak *et al.*, 1997] of positive and negative fluctuations in reflectance and transmittance fields. Numerical 3D radiative transfer helps us interpret these fluctuations as geometrical shadowing effects that dominate in broken cloud scenes and/or the radiative smoothing effects that dominate in completely overcast situations (where variability still occurs *inside* the cloud layer). The cancellation occurs in the common illumination/viewing geometry (that will apply to most MTI observations), but *not* for near-zenith sun [Davis *et al.*, 1998] where they are however smaller in magnitude.

We can also say that ...

> *at scales of interest in many remote-sensing applications*, the standard (homogenous plane-parallel) cloud model *per se* is generally inapplicable. What can be done with this model is to infer "effective" cloud properties, i.e., properties that give the observed radiance but that

are generally different from the pixel-averaged cloud property that we would really like to know —this is the strategy in MODIS cloud products.

Currently, there is a considerable amount of research under way aimed at quantifying errors related to operational "independent-pixel approximations" (IPAs) in remote-sensing [e.g., Chambers *et al.*, 1997; Davis *et al.*, 1997] and correcting them approximately [Marshak *et al.*, 1998].

11. 2. 2 An MTI Perspective on Cloud Radiative Transfer

Since there will be no (routine) attempt to infer cloud parameters from MTI radiances, we can fall back on the simple definition of clouds as highly reflective/emissive objects. If the observation is in day-time, a cloud's signature is uniformly high BRDFs across the VIS/NIR spectrum where the atmosphere is highly transparent (channels A–F). If the observation is by night, the thermal IR signature of cloud (top) is a lower brightness temperature than the surface, due to the thermal stratification of the atmosphere.

These simple criteria are not fool-proof; for example, snow-cover is bright and cold. This is a case where the two-view sampling of MTI targets could prove useful. As part of the (level 4) projected cloud-shadow mask production, we can infer by triangulation the altitude of the bright/cold object above WGS84 or DEM (if available); if it is significantly above ground, it is surely a cloud and not snow. Alternatively, one can use a "slicing" technique. There can be other high-albedo components in a scene than clouds and snow, e.g., gypsum and painted surfaces. Generally speaking, clouds can be distinguished from snow and other bright surfaces one or more of the following characteristics [cf. Goodman and Henderson-Sellers, 1988; Rossow and Garder, 1993; Gustafson *et al.*, 1994]: relatively large spatial extent, higher altitude (hence colder), lack of correlation with land surface features, and dynamic behavior. For instance, how do we identify dense fog in a snowy region? Apparently, snow is darker in MWIR region (channels J,K).

11.3 Algorithm Steps

The foregoing remarks push us towards working only with cloud-free images. If clouds where not so frequent, this would be a viable strategy. Because they are so frequent, we are compelled to make heroic efforts to "see through" holes in the cloud cover. The following semi-interactive procedure is about as complicated as one would ever want to get. How far it actually will be taken depends on intermediate results.

Cloud masks for nadir- and 60°-views are initialized at 0.

1) Is this a day-time scene? If not, skip next step.

2) If so, the calibrated multi-spectral nadir image is scanned for exceeding a threshold in BRDF. [The cloud-type, wavelength- and geometry-dependent thresholds can be aligned with those used for MODIS at the highest level of confidence for cloud occurrence.] If the criterion is fulfilled, set the cloud-bit to 1 for the pixel under examination.

3) The calibrated multi-spectral nadir image is scanned for not exceeding a threshold in brightness temperature. [Same remark about MODIS thresholds here.] If the criterion is fulfilled, set the cloud-bit to 1 if it is 0. If the test is failed and the cloud-bit is already 1 (a certain number of times?), stop procedure and alert the operator about this inconsistency.

4) Repeat last two steps with 60°-view.

The above steps, corresponding to a standard (level 2) cloud-mask production, are summarized in Fig. 11-1a. See Fig. 11-2 for a MAS-based illustration of the above steps using wavelengths close to MTI's channels C (red), I (SWIR), and N (LWIR). The remainder is a research project; it feeds back into the standard cloud mask to discriminate cloud and snow, and then produces new (level 4) "cloud shadow" masks.

5) Count/identify clouds in nadir view. If there are more than a certain number, abort procedure and alert the operator. Otherwise, do this for the 60°-view sub-image that overlaps the nadir scene, then decimate the sub-image to bring it to the same ground resolution as for nadir.

6) Produce a mapping between individual clouds in nadir and 60° views by seeking maximum overlap of the two cloud masks. To do this, the clouds must be individually advected forward and/or backward using horizontal wind inferred by hand-watching one or more clouds. Clouds can be advected in and out of the 12×12 km scene during the 7 min. between views; so some clouds will not have stereo pairs. Of the remainder, there should not be so many "no hit" or "multiple hit" cases that they cannot be resolved by visual examination. Use navigational data to find individual cloud heights by triangulation.

7) If any clouds occur very close to ground, alert the operator. He/she can either reset the cloud-bit to 0 in both views if the likelihood is that the target is snow, otherwise leave it at 1 to flag a dense fog.

If the terrain is not flat (within limits to be determined), nor is there a digital elevation model (DEM) available, then pass images and cloud masks to the next step (aerosol corrections). If the topography is flat or known, set two more "cloud-shadow" masks to 0 and ...

8) Compute for each cloud its geometrical shadow on the terrain, and set the cloud shadow mask value to 1 within the shadow at both nadir and 60° viewing.

This cloud-shadow mask will inform subsequent surface property retrievals using VIS/NIR channels about potential for significant error. See Fig. 11-1b for a summary.

11.4 Error Budget

To minimize errors that will occur "down the road" (that the MTI image-pair is traveling), it is better to err on the conservative side in cloud detection. A first precautionary measure in this direction is to "grow" an individual cloud in the mask into its convex hull.

11.5 Validation Plan

MTI glimpses at the ARM site in Oklahoma (Central Great Plains CART) will provide a means to validate the cloud mask, most importantly for broken cloud fields. The central facility has an all-sky camera that can be used, in conjunction with the co-located cielometers, to triangulate clouds by day as well as by night (via obstruction of stars which are in predictable positions).

11.6 Software Implementation Plan and Status

An IDL procedure that executes steps 1-4 in Section 3 is in the planning stage. Depending on success and demand, further steps will be implemented and tested.

Desirable test-images: cloud-contaminated LANDSAT, SPOT, MAS and/or AVIRIS data. Several images from the latter have been ordered.

11.7 Product Summary

In this chapter, we report on how the Level 2-CldM ("Non-Cirrus" cloud mask) in Table 1-2 is produced. This mask is binary and flags pixels where a cloud is obstucting the view angle. Input to this procedure is one or more VNIR or TIR Level 1B (registered/calibrated) scenes, along with associated thresholds.

We also describe how a more advanced product (tentatively assigned to Level 4) could be generated: a "cloud-shadow" mask. This is simply the counterpart of Level 2-CldM for solar angle; however, it's production is not as easy.

References

Cess, R. D., M. H. Zhang, Y. Zhou, X. Jing, and V. Dvortsov, 1996: "Absorption of solar radiation by clouds: Interpretations of satellite, surface and aircraft measurements," *J. Geophys. Res.*, **101**, 23299–23309.

Chambers, L., B. Wielicki, and K. F. Evans, 1997: "On the accuracy of the independent pixel approximation for satellite estimates of oceanic boundary layer cloud optical depth," *J. Geophys. Res.*, **102**, 1779–1794.

Davis, A., A. Marshak, R. F. Cahalan, and W. J. Wiscombe, 1997: "The LANDSAT scale-break in stratocumulus as a three-dimensional radiative transfer effect, implications for cloud remote sensing," *J. Atmos. Sci.*, **54**, 241–260.

Davis, A., A. Marshak, R. F. Cahalan, and W. J. Wiscombe, 1998: "Insight into three-dimensional radiation transport processes from diffusion theory, with applications to the atmosphere," In

Proceedings of International Symposium on Radiative Transfer, July 21–25, 1997, Kusadasi (Turkey), to appear at Begell House, New York (NY).

Goodman, A. H., and A. Henderson-Sellers, 1988: "Cloud detection analysis – A review of recent progress," *Atm. Res.*, **21**, 203–.

Gustafson, G. B., R. G. Isaacs, R. P. d'Entremont, J. M. Sparrow, T. M. Hamil, C. Grassotti, D. W. Johnson, C. P. Sarkisian, D. C. Peduzzi, B. T. Pearson, V. D. Jakabhazy, J. S. Belfiore, and A. S. Lisa, 1994: "Support of Environmental Requirements for Cloud Analysis and Archive (SERCAA) – Algorithm descriptions," Phillips Laboratory Scientific Report No. 2, 100 pp, Hanscom Air Force Base (Ma).

Imre, D. G., E. H. Abramson, and P. H. Daum, 1996: "Quantifying cloud-induced shortwave absorption: an estimation of uncertainties and of recent arguments for large excess absorption," *J. Appl. Meteor.*, **35**, 1991–2010.

Marshak, A., A. Davis, W. J. Wiscombe, and R. F. Cahalan, 1997: "Inhomogeneity effects on cloud shortwave absorption measurements: Two-aircraft simulations," *J. Geophys. Res.*, **102**, 16,619–16,637.

Marshak, A., A. Davis, R. F. Cahalan, and W. J. Wiscombe, 1998: "Nonlocal independent pixel approximation: direct and inverse problems," *IEEE Trans. Geosc. & Remote Sens*, **36**, 192–*205*.

Rossow, W. B., and L. C. Garder, 1993: "Cloud detection using satellite measurements of infrared and visible radiances for ISCCP," *J. Climate*, **6**, 2341–2369.

Wharton, S. W., and M. F. Myers (Eds.), 1997: *MPTE/EOS Data Products Handbook, Vol. 1: TRMM & AM-1*, pp. xvi+265, available from: NASA's Goddard Space Flight Center (Code 902), Greenbelt (Md), USA.

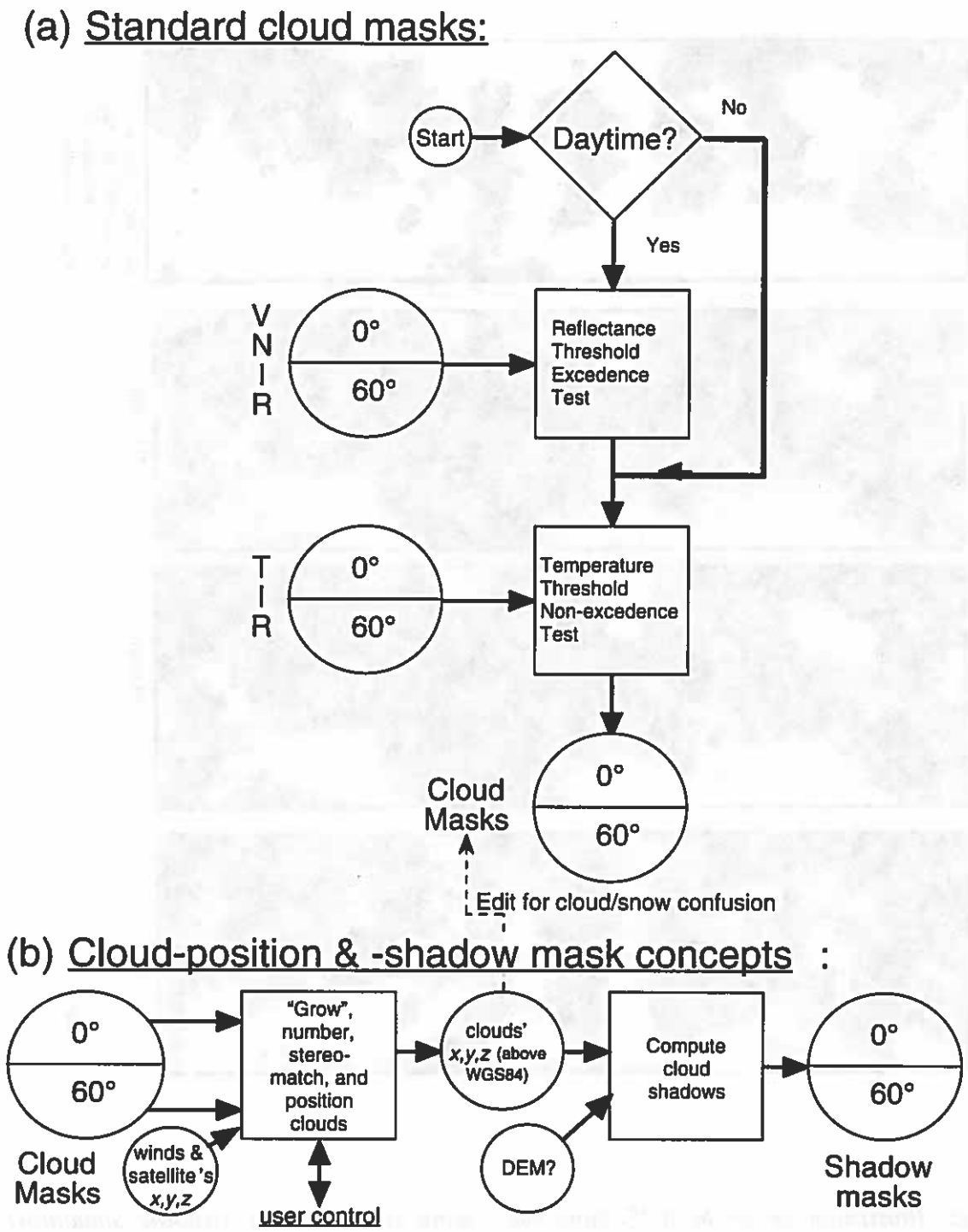

Figure 11-1: *Flow chart for the MTI cloud mask algorithm.* **(a)** Production of level-2 cloud mask for viewing geometry; **(b)** same for level 4 cloud-mask for illumination geometry (cloud-shadow mask).

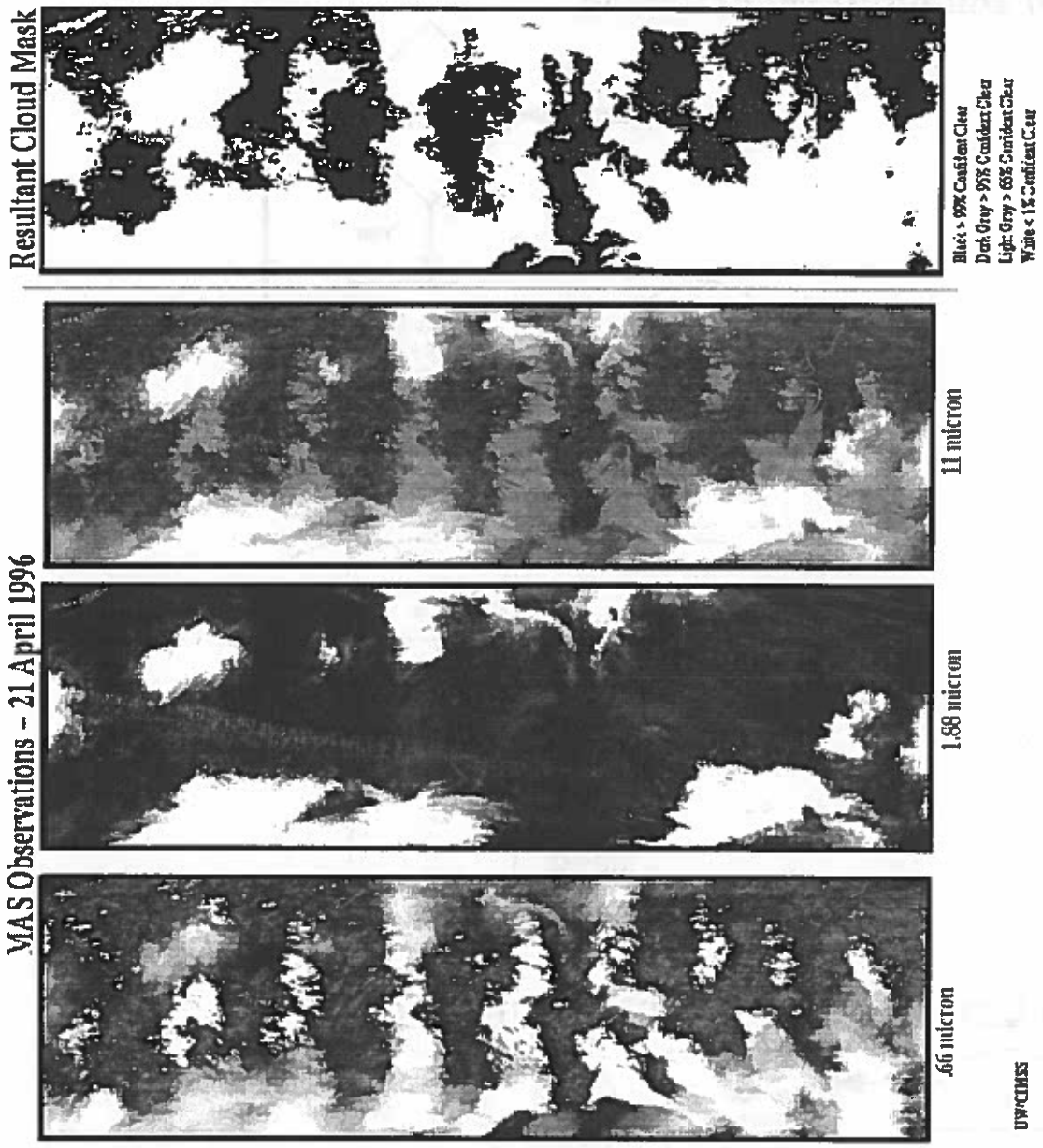

Figure 11-2: *Illustration of the MODIS cloud mask using MAS (MODIS Airborne Simulator) data.* From left to right: three images for wavelengths than can be assimilated to MTI's channels C, I, and N, followed by the resulting cloud mask. Due to its higher spatial resolution, we do not anticipate the need for a cloud mask with 4 shades of gray for MTI, just on/off.

12. THIN CIRRUS DETECTION/REMOVAL

Anthony B. Davis

12.1 Introduction and Goal

Cirrus (Ci) are one of the most frequent cloud types, so much so that they share the attention of climate modelers (when they actually do focus on clouds) with the vast, dense and persistent boundary-layer phenomena known as marine strato-cumulus. Ci however form at high altitudes, typically just below the tropopause (10–18 km); they consist of ice crystals, often with complex shapes. Unlike boundary-layer clouds, Ci are generally quite thick (1–2 km) but are never totally opaque; like boundary-layer clouds, Ci are highly heterogeneous in space and variable in time. In the same way as ship-tracks produce/modify marine boundary-layer clouds, aircraft contrails add to the frequency and texture of Ci in ways which are currently under investigation.

If a Ci layer is dense enough to activate the cloud mask (cf. previous chap.), not much else can be done with respect to surface observation. If not, there still may be thin ("sub-visual") Ci present [Lynch, 1993] and there is a recently–introduced remedy for this situation, at least for daytime observations [Gao *et al.*, 1993, 1997].

The goal of the algorithm described in this report is to detect the presence of thin Ci in otherwise "clear-sky" scenes or sub-scenes. Having found a thin-Ci signature, the next step is to remove the Ci effect in the pixel–reflectance value. This is the first of two atmospheric correction procedures, the second tracks the effect of tropospheric aerosol in the image (cf. Section 13).

There is one major similarity and a number of differences between the Ci and aerosol correction procedures. The similarity is the need for a dark (low-reflectivity) surface feature to isolate as well as possible the atmospheric signal. A first difference is that, for the aerosol, a dark feature is sought spatially in the image (preferably a body of water and the larger it is, the better) whereas, for the Ci, the dark feature is sought spectrally, and found by design in channel H (1.36–1.39 μm) that lies in a relatively narrow H_2O absorption band. The absorption features for ice do not coincide with those of water in its vapor phase, so Ci scatter sunlight in channel H. In summary, the atmospheric boundary-layer and lower troposphere, are generally —but not systematically— loaded with enough water-vapor to completely block direct sunlight to the ground; they therefore act like a dark "surface" below the more-or-less reflective Ci layer.

Another difference between aerosol and Ci is that, to some extent, we have knowledge of the aerosol scattering phase-function; this is far from true for Ci where the scatterers are ice crystals with complex shapes and, often, preferred orientations ("sun-dogs" are witness to this). Phase functions have been computed for the simpler habits (hexagonal plates and cylinders), generally

with random orientations) in the geometrical–optics limit (large particles). Progress is under way for more complicated (fractal-like) geometry and moving away from the asymptotic (large size parameter) regime. At any rate, the phase function issue is enough of a complication in the radiative transfer that the empirical approach described below is better justified than an attempt to model the signal physically (using, e.g., a 6S-type code).

Finally, there is a significant difference in the potential for pixel adjacency effects in aerosol and in Ci due to their broad separation in altitude. The contrast between a small body of water and its immediate (and, hopefully, uniform) environment can actually be used to determine aerosol optical depth by quantifying the adjacency effects [Royer *et al.*, 1989]; in turn, this atmospheric parameter can be used to inform the atmospheric correction scheme for the satellite image either locally or globally to remove aerosol effects (cf. Section 13). For Ci, adjacency effects will involve quite large distances on the ground so surface homogeneity assumptions are more highly questionable than for aerosol. Modeling and exploiting adjacency effects in Ci layers is out of our scope, for the time being.

12.2 Scientific Basis

12. 2. 1 Resolved Issues

MTI's channel H was specifically designed to implement Bo–Cai Gao's thin Ci detection- and removal schemes. Channel H two-way transmission is plotted vs. altitude in Fig. 1 for two standard atmospheric profiles. Since ground and lowermost atmospheric layers are, for all practical purposes, not illuminated in channel H, the reflected sunlight is produced by high-altitude scatterers: ice particles in Ci, and stratospheric aerosol (plus, for completeness, a residual of Rayleigh scattering). In the following empirical algorithm it is not important to separate these components. Experience shows that, when present, sub-visual Ci dominate and, furthermore, fluctuate over a satellite scene [Gao and Kaufman, 1995]; this will be true for MTI scenes.

A histogram-and-threshold method can be used to detect the presence of thin Ci with calibrated channel H reflectances. We can align our choice in threshold to MODIS values with a somewhat increased confidence than for the EOS–AM instrument, due to the better spatial resolution; see *MPTE/EOS Data Products Handbook, Vol. 1, TRMM & AM-1* [Wharton and Myers, 1997; and references therein].

Ci contamination of VIS/NIR channels (channels A–F) can be removed, by daytime at least. Following Gao *et al.* [1997], we assume for Ci in isolation a simple linear relation between the Bi-directional Reflectance Distribution Function (BRDF) values at 1.38 μm (above some threshold ρ_{Ci}^*) and another wavelength λ:

$$\rho_{Ci}(\lambda) = K_\lambda \times [\rho_{Ci}(1.38) - \rho_{Ci}^*], \tag{12.1}$$

for $0.4 \leq \lambda \leq 1.0$ μm, noting that Gao *et al.* assume implicitly that $\rho_{Ci}^* = 0$. This modification is required in situations where the atmosphere is particularly dry and/or the target is high in altitude.

We now seek "surface" reflectance $\rho_{sfc}(\lambda)$ in the standard decomposition

$$\rho^*(\lambda) = \rho_{Ci}(\lambda) + T_{Ci}(\lambda) \times \rho_{sfc}(\lambda) \qquad (12.2)$$

where the l.h.s. is the observed BRDF and $T_{Ci}(\lambda)$ is the two-way transmittance of the Ci layer. In this picture, we view the "surface" as the atmosphere-ground system below the Ci which is assumed horizontally uniform, and we have neglected multiple reflections between the Ci layer and the sub-Ci strata.

To find K_λ, we use channel H vs. channel X scatter-plots, X spanning A–F (maybe G too). A regression is done between channel H values (attributed to Ci) and the lower envelop of channel X values at a given channel H value (attributed to the Ci contamination); see Fig. 2. Knowing K_λ, we can solve Eqs. (12.1–2) on a pixel-by-pixel basis for $T_{Ci}(\lambda) \times \rho_{sfc}(\lambda)$, the "Ci-path-radiance-corrected" image; see Figs. 12-3a–c). The $T_{Ci}(\lambda)$ factor is not well-known (see below) but can be assumed ≥ 0.9.

12. 2. 2 Unresolved Issues, and MTI-Specific Resources to Address Them

The above "state-of-the-art" Ci removal scheme falls short of providing $\rho_{sfc}(\lambda)$ to the next step of the image processing, namely, further atmospheric correction for aerosol effects. Being empirical in nature, the scheme does not yield the two-way transmission factor $T_{Ci}(\lambda)$ in Eq. (12.2). Gao *et al.* [1997] have tried *ad hoc* connections of the form $T_{Ci}(\lambda) = [1-\rho_{Ci}(1.38)]^{n(\lambda)}$ with $1 \leq n(\lambda) < 2$ without much success to date. Another parameterization proposed by C. Borel, based on a λ-dependent linear relation between $1-T_{Ci}(\lambda)$ and $\rho_{Ci}(1.38)$, will be tested.

More importantly: How do we detect/remove Ci in night-time observations, using thermal IR channels only? Preliminary computations by Tornow and Borel [1994] suggest that this is possible using the well-calibrated thermal radiometry available from MTI.

A problem area, related on physical grounds to the above transmission problem because of emissivity effects, is: How to correct for the Ci contamination in the thermal IR channels (J–N)? Note that the "robust" water temperature retrieval (Section 6) works even in presence of thin cirrus [Tornow and Borel , *op. cit.*].

We have some resources to address the above questions that are specific to the MTI instrument and platform: two views of the same scene at a some time–interval ($\approx$6 minutes) and wide viewing-angle separation (nadir and 60°); high radiometric resolution and excellent calibration in the thermal IR. This last feature is where hope lies for night-time observations. NASA's MODIS instrument team has sanctioned a relatively standard Ci detection scheme using spatial/spectral contrast signatures in the thermal regions [d'Entremont, 1993; and references therein]. However, this scheme feeds a cloud-parameter retrieval rather than an atmospheric correction. Unfortunately, the

scheme works only for relatively *dense* Ci layers; its break-down for *tenuous* Ci is traceable primarily due to limited radiometric resolution (B.-C. Gao, private communication).

12.3 Algorithm Steps

- Histogram and visualize (clear-sky portion of) channel H image. Is there evidence of Ci?
- If not, proceed to correction for aerosol contamination of surface BRDFs (following chapter). If so, set a threshold above which the signal is believed to be Ci-only and proceed to next step. Exceedence of this threshold defines the binary thin-Ci cloud mask (Level 2-CiM) in Table 1.2. The remainder of this algorithm is considered optional (level 4).
- Determine K_λ's for all desired VIS/NIR channels, using the scatter-plot technique (modified to be "above-threshold" in channel H).
- Produce Ci-path-radiance-corrected image, using Eqs. (12.1–2).
- Choose two-way transmission factor locally (*ad hoc* relation?) or globally (climatology?) and produce Ci-corrected image pixel-by-pixel.

Proceed to aerosol correction (next chapter) to obtain surface BRDFs.

12.4 Error Budget

This is a situation where doing anything is better than nothing but the sources of error in the final outcome are numerous and difficult to estimate at this point in time. Overall BRDF accuracy is probably degraded to about 5–10 % if Ci removal is required.

12.5 Validation Plan

MTI glimpses at the ARM site in Oklahoma (Central Great Plains CART) will provide a means to validate atmospheric correction in general, Ci removal in particular. The central facility has a micro-pulse lidar, which is sensitive enough to detect sub-visual Ci layers and there will be, hopefully at close time intervals, cases with and without Ci events.

Desirable test-images: AVIRIS and/or MAS (MODIS Airborne Simulator) data with thin cirrus. We already have the former type of data (captured during FIRE II over Kansas) from archives.

12.6 Software Implementation Plan and Status

An IDL procedure that executes the steps described in Section 3, with supervision, is in the planning stage. We will investigate some ideas about how to automate the channel H threshold choice.

12.7 Product Summary

In this chapter, we report on how the Level 2-CiM ("Cirrus" cloud mask) in Table 1-2 is produced. This mask is binary and flags pixels which are significantly contaminated by path-radiance created by light scattering in their (sub-visual) Cirrus layers. The input to this procedure is a Level 1B scene in channel H and a threshold value. This threshold will likely be tuned by the user to each situation, e.g., if the target is in a high/dry area.

We also describe a Level-4 procedure for removing the Cirrus contamination using an empirical technique pioneered by Bo-Cai Gao and co-workers.

References

d'Entremont, R. P., 1993: Detection and Analysis of Cirrus Clouds Using Passive Infrared Satellite Data, *S.P.I.E. Proceedings*, *vol. 1558*, Ed. D. K. Lynch, pp. 164–179, 1993.

Gao, B.–C., A. F. H. Goetz, and W. J. Wiscombe, 1993: Cirrus Cloud Detection from Airborne Imaging Spectrometer Data Using the 1.38 µm Water Vapor Band, *Geophys. Res. Lett.*, **20**, 301–304.

Gao, B.–C., and Y. J. Kaufman, 1995: Selection of 1.375-µm Channel for Remote Sensing of Cirrus Clouds and Stratospheric Aerosols From Space, *J. Atmos. Sci.*, **52**, 4231–4237.

Gao, B.–C., Y. J. Kaufman, W. Han, and W. J. Wiscombe, 1998: Correction of Thin Cirrus Path Radiance in the 0.4–1.0 µm Spectral Region Using the Sensitive 1.375 µm Cirrus Detecting Channel, *J. Geophys. Res. – Atmospheres* (submitted).

Lynch, D. K., 1993: Subvisual Cirrus: What it is and where you find it, *S.P.I.E. Proceedings*, *vol. 1558*, Ed. D. K. Lynch, pp. 264–274, 1993.

Royer, A., A. Davis, and N. O'Niell, 1989: Analyse des effets atmosphÈriques dans les images HRV de SPOT. *Can. J. Remote Sens.*, **14**, 80–91.

Tornow, C., and C. C. Borel, 1994: Multi-angular multi-spectral night-time water temperature retrieval, in *MTI Technical Report* (MTI-94-001).

Wharton, S. W., and M. F. Myers (Eds.), 1997: *MPTE/EOS Data Products Handbook, Vol. 1: TRMM & AM-1*, pp. xvi+265, available from: NASA's Goddard Space Flight Center (Code 902), Greenbelt (Md), USA.

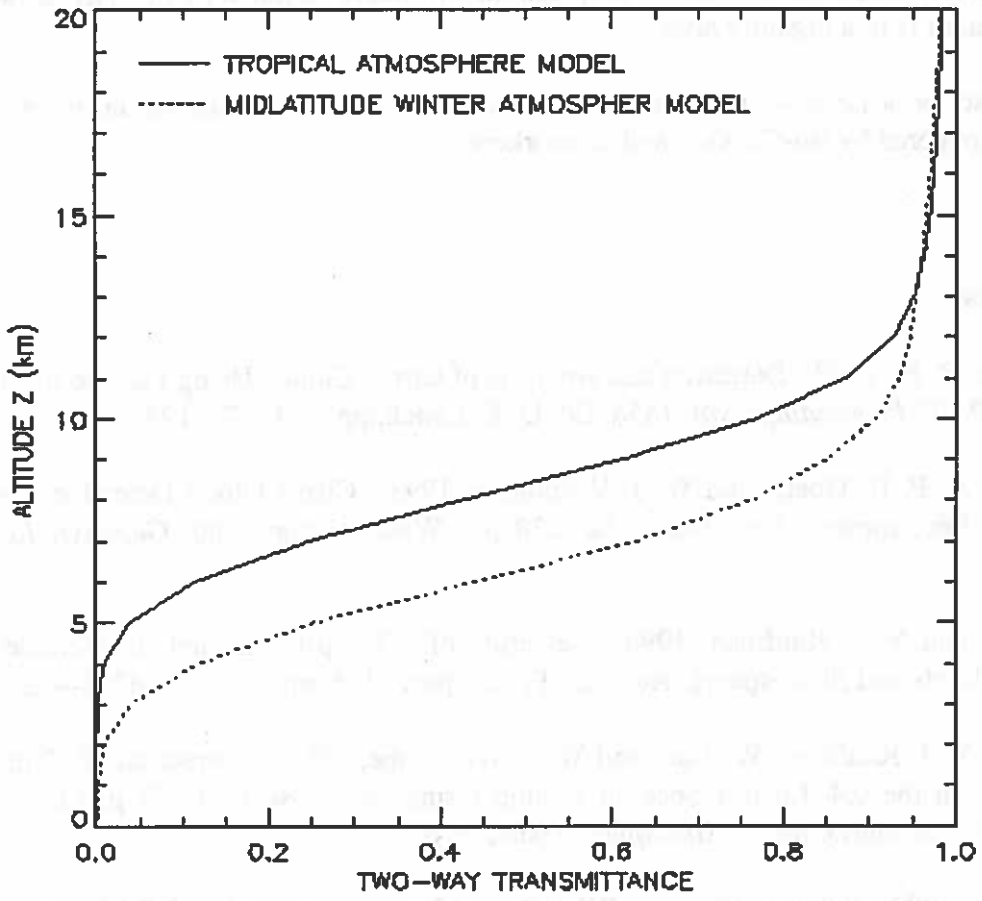

Figure 12-1: *Two-way transmission in the 1.36–1.39 μm spectral region (channel H) from TOA to altitude z.* Two standard atmospheric models are used: tropical and mid-latitude winter.

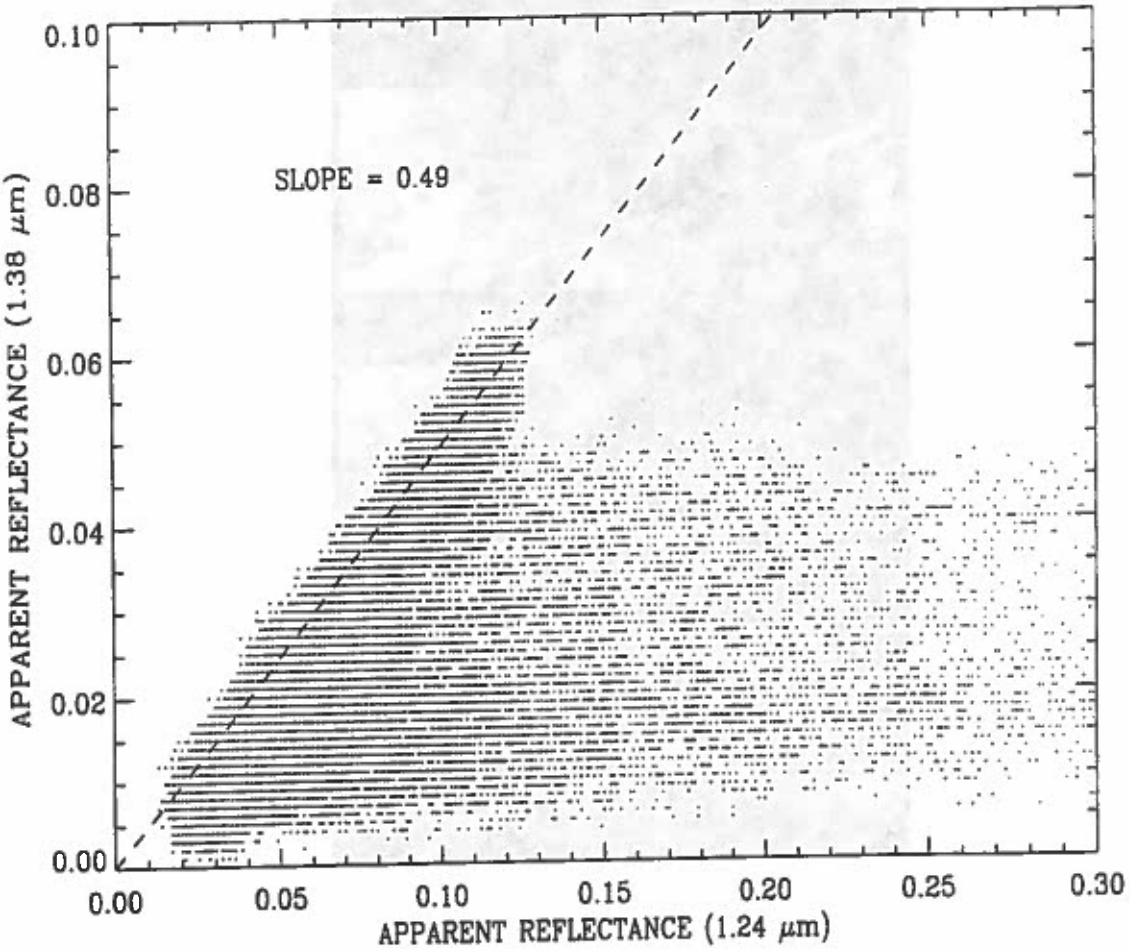

Figure 12-2: *Two-wavelength scatter plot: 1.38 μm vs. 1.24 μm.* AVIRIS data from the Gulf of Mexico was used. Reproduced from Fig. 4 in Gao *et al.* [1998], courtesy of Bo–Cai Gao.

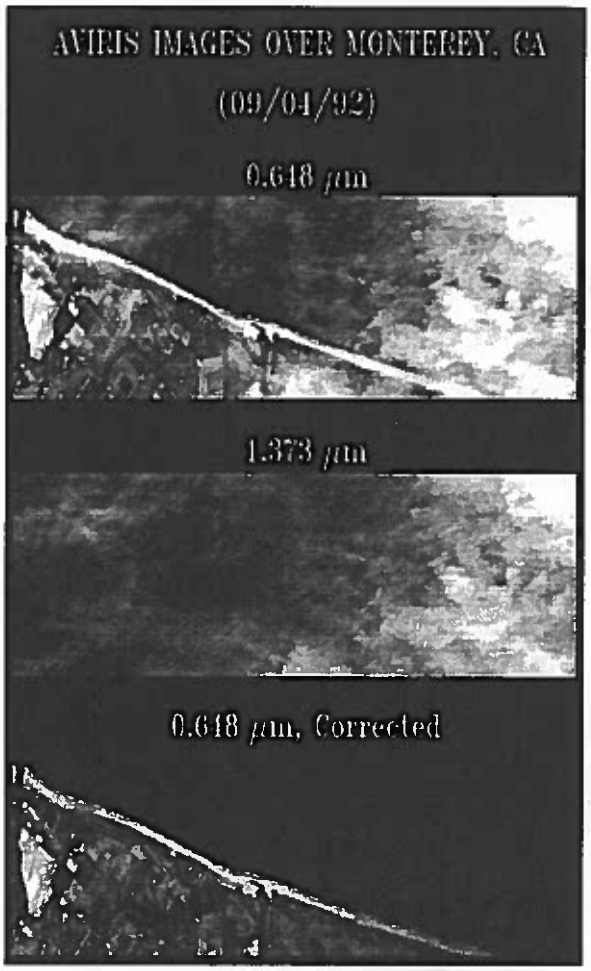

Figure 12-3: *Thin-cirrus correction of an AVIRIS image of the California Coast, near Monterey.* (*a*) raw data at 0.65 µm. (*b*) data at 1.37 µm (≈ Channel C). (*c*) corrected data at 0.65 µm (≈ Channel H). Reproduced from Fig. 8 in Gao *et al.* [1998], courtesy of Bo–Cai Gao.

13. SCATTERING AND ABSORPTION BY AEROSOLS

Pierre V. Villeneuve and Christoph C. Borel

13.1 Algorithm Objective

The goal of this algorithm is to correct the MTI visible and near-infrared channels for the aerosol path radiance to give true ground reflectance.

13.2 Scientific Basis

The principle of this atmospheric correction method (Liang 1997 and Fallah-Adl 1997) is based on radiative transfer theory. As indicated in Figure 13-1, for a plane-parallel atmosphere bounded by a Lambertian surface, the measured radiance at the top of the atmosphere can be expressed as

$$L_m = L_{up} + \frac{\rho F_d t}{\pi(1 - S\rho)} \qquad (13\text{-}1)$$

where L_{up} is the upward path radiance, ρ is the surface reflectance, F_d is the downward diffuse and direct flux at the ground, t is the transmittance from the surface to the sensor, and S is the atmospheric spherical albedo. The one-dimensional assumption is not a serious problem compared to other assumptions made. The objective of the aerosol correction algorithm is to retrieve the surface reflectance ρ from the observed radiance L_m. Most quantities in Equation 13-1 are functions of the optical properties of the atmosphere.

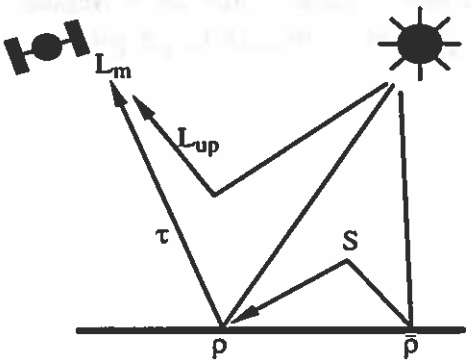

Figure 13-1. Components of TOA-measured radiance.

There are two important steps to any operational atmospheric correction algorithm. These are the retrieval of optical properties from the imagery itself, and calculating the surface reflectance from the imagery and retrieved parameters. In this algorithm, the only variable that is estimated from the image data is the aerosol optical thickness. Other parameters are determined on the basis of the specific aerosol model and on the climatological conditions that exist. Many of the parameters needed to run an atmospheric code are readily known or can be easily computed, such as the solar illumination and sensor viewing geometries and atmospheric Rayleigh optical depth. However the aerosol optical depth varies significantly both spatially and temporally and must be determined on a scene-specific basis.

Our plan is to use a look-up table (Fraser 1992) using dark targets as a source of aerosol optical depth. Over extended dark targets such as dense forest and water bodies the majority of the measured radiance will be due to aerosol-reflected solar radiance. The areas must be on the order of 1 km in size in order to avoid scattered light from adjacent bright areas.

Dark targets with very low reflectance in the visible region are useful in this application because any uncertainties in the assumed dark target reflectance will have a minimal effect on the retrieved aerosol optical thickness (Teillet and Fedosejevs 1995). Also, dark surfaces such as clear water and dense green vegetation will be common for our application.

13.3 Algorithm Steps

The algorithm to correct TOA measurements of radiance (or reflectance) for atmospheric aerosol effects to give surface reflectance is a two step process. The first is to estimate the atmospheric aerosol optical depth from the visible and shortwave IR scene data itself, and the other is to calculate surface reflectance given aerosol optical depth and TOA measurements. The individual steps of this algorithm are illustrated as a flowchart in Figure 13-2.

The primary inputs to this algorithm are the co-registered geo-located TOA radiance data (Level 1B-R-Geo) in all bands except the five thermal channels, and the normalized difference vegetation index (Level 2-NDVI). Ancillary input data includes satellite viewing angles, scene-local solar angle and a pre-calculated 6S (Vermote et al, 1997) look up table.

Observations (Kaufman 1996) have shown that reflectance values in the MTI channels A and C correlate highly with channel O surface reflectance for dense vegetation canopies and dark soils. Thus once ρ_O has been determined, ρ_A and ρ_C in dark target pixels are calculated as $\rho_A = 0.25\ \rho_O$ and $\rho_C = 0.50\ \rho_O$.

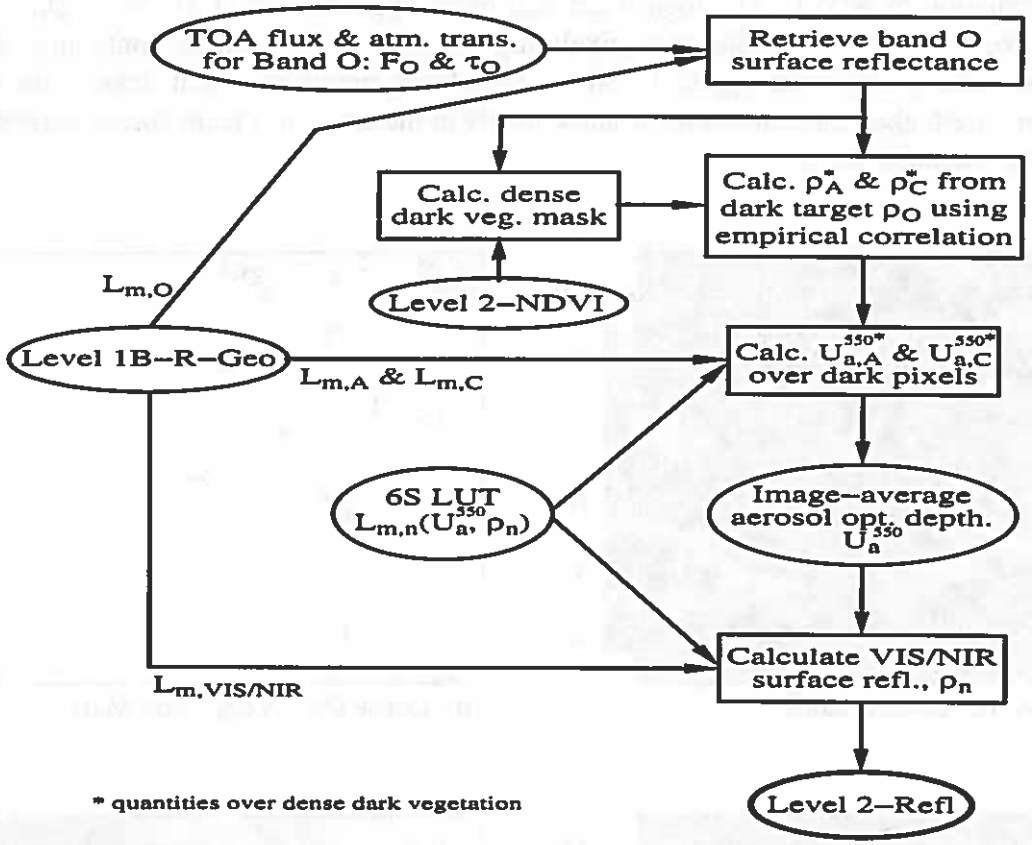

Figure 13-2. Aerosol correction algorithm flow chart.

An AVIRIS dataset resampled to MTI channels will be used in an example of applying the atmospheric aerosol correction. This AVIRIS flight was from an overflight of Camarillo, CA in May of 1995, which is an area of predominantly farm land bordered with mountains and is located several miles from the Pacific ocean. The AVIRIS hyperspectral data cube was resampled to the ten MTI visible and near infrared bands A - I and O in units of reflectance. The AVIRIS instrument is typically flown at high altitudes and thus the measured quantities are assumed to be equivalent to TOA measurements. Band A of this scene is shown in Figure 13-3(a) expressed in reflectance.

The first step of the aerosol optical depth calculation is to determine which groups of scene pixels qualify as dense dark vegetation. These pixels are important since they will be used in the prediction of surface reflectance ρ_A and ρ_C from ρ_O. Band O surface reflectance is easily determined by normalizing the TOA band O radiance by the incident solar flux since atmospheric transmission and absorption are negligible (Holben, 1992) at this wavelength (2.2 μm). Dark scene pixels are found by noting which pixels in this image are below a certain threshold. In this example case a reflectance threshold of 0.15 was used. Thus all pixels with a reflectance lower than 0.15 were selected as being sufficiently dark. The next step was to identify which of these pixels also corresponded to dense vegetation. For this step a lower threshold of 0.5 was used on the normalized difference vegetation index (NDVI) to identify pixels containing dense vegetation. In this example NDVI was calculated from the TOA reflectances in bands C and D. See Chapter 15 for more details

on the calculation of NDVI. The logical product of an upper threshold (0.15) on ρ_O and a lower threshold (0.5) on NDVI results in a pixel map of those scene pixels containing dense dark vegetation. This is shown in Figure 13-3(b), where black pixels represent dense dark vegetation. Notice there are higher concentrations of black pixels in the upper left hand corner corresponding to the forested mountain slopes.

(a) Band A TOA Reflectance

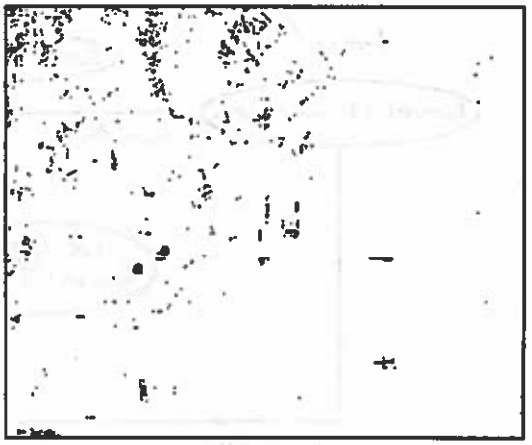

(b) Dense Dark Vegetation Map

(c) Band A Surface Reflectance

(d) Band A TOA Refl.– Surface Refl.

Figure 13-3. Example application of aerosol correction algorithm.

The next step is to estimate surface reflectance in Bands A and C from the calculated Band O surface reflectance. Surface reflectances ρ_A and ρ_C are necessary for the calculation of atmospheric aerosol optical depth. Observations (Kaufman, 1996) have shown that reflectance values in the MTI channels A and C correlate highly with channel O surface reflectance for dense vegetation canopies and dark soils. Thus once Band O surface reflectance has been determined, ρ_A and ρ_C in the dark target pixels are calculated as $\rho_A = 0.25\ \rho_O$ (±30%) and $\rho_C = 0.50\ \rho_O$ (±17%). The uncertainties for these two expressions are relatively large, but their overall effect is diminished since the

reflectivities are themselves very low as this relation is only applied to the previously identified dense dark vegetation pixels.

At this point for each of the dense dark vegetation pixels we now know both the surface reflectance and the TOA reflectance in bands A and C. From this it is possible to calculate the atmospheric aerosol optical depth, given a few simplifying assumptions about the conditions of the atmosphere. This is done using a comprehensive look up table (Fraser, 1992) relating TOA radiance (or TOA reflectance), surface reflectance, aerosol optical depth, wavelength, solar zenith angle, viewing zenith angle, and relative azimuth angle. This look up table may be calculated from any number of accepted atmospheric radiative transfer models. In this case we chose 6S (Vermote, et al, 1997) because of it's ability to include surface bidirectional reflectance models in it's calculations. Since MTI will observe each earth scene from two viewing directions, we must account for bidirectional effects in order to make comparisons between the two looks.

An example of a portion of the look up table (LUT) for the Camarillo AVIRIS scene for MTI Band A is shown in Figure 13-4, giving TOA reflectance versus surface reflectance for a range of aerosol optical depths at a wavelength of 0.55 μm. The 6S model parameterizes aerosol optical depth at a single optical depth and the aerosol optical depths at other wavelengths are calculated from a functional relation (Liang, 1997). It is now possible to calculate from this LUT the aerosol optical depth over the dense dark vegetation pixels since the TOA reflectance are known from the measurements and we have estimated the surface reflectance in band A from a simple correlation. A similar process is done with Band C reflectances and a corresponding set of entries in the LUT. The result of each of these interpolations through the LUT is a pair of estimates, for each dark pixel, of the aerosol optical depth at 0.55 μm which are averaged together to give a final aerosol optical depth valid for the entire scene (not just the dark pixels). In the example presented here the aerosol optical depth at 0.55 μm was found to be 0.201.

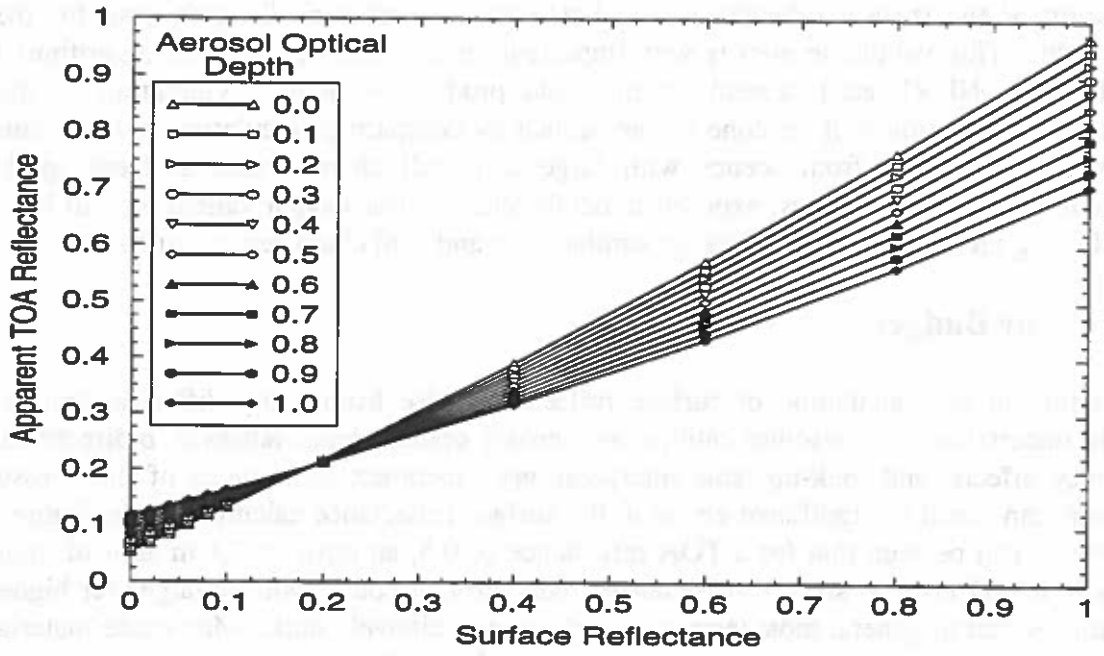

Figure 13-4. MTI Band A 6S look up table.

The second part of this algorithm is to use the above-calculated aerosol optical depth (0.201 in the example) to calculate the surface reflectance at each pixel using the 6S LUT, given the TOA reflectance (or radiance). For each scene pixel an interpolation is performed within the LUT for the measured TOA reflectance, the calculated aerosol optical depth, and the proper viewing and illumination angles. The resulting predicted surface reflectance from the AVIRIS-based scene example is shown in Figure 13-3(c). Notice that, in comparison with the TOA reflectance in Figure 13-3(a), now there is a much strong contrast between light and dark areas. The difference between TOA reflectance and calculated surface reflectance is shown in figure 13-3(d). The difference is highest over dark areas (mountain slopes and certain fields) because it is over these dark surfaces that the atmospheric path contribution is most significant. There is very little change over the bright field in the lower center of the scene, since the surface reflectance was approximately 0.25. As can be seen from Figure 13-4, there is a crossover point at these values of surface reflectance where scattering by aerosols into the path and out of the path are comparable.

13.4 Validation Plan

There are two parts to the validation of the atmospheric correction algorithm. The first is to validate the calculation of the scene aerosol optical depths. There are numerous possibilities for this task. Before launch this will be done with MTI data simulated from AVIRIS and MAS cubes from overflights of any of the AERONET network of sunphotometers (Holben, 1996). This worldwide network of instruments was established by the NASA EOS program for the purpose of providing ground truth for the soon to be launched EOS AM-1 carrying MODIS, MISR, and ASTER, among others. After MTI launch further validation of the aerosol calculation will be done by placing one or more of our own sunphotometers within MTI ground scenes.

Validation of the surface reflectance calculation will be more challenging than for the aerosol calculation. This validation step is very important since a number of other algorithms (material identification, NDVI, etc.) depend on this data product as input. Validation of the surface reflectance calculation will be done before launch by comparing calculations with simulated data (AVIRIS, MAS, etc.) from scenes with large and well characterized surfaces (parking lots, warehouse roofs, water bodies, exposed minerals, etc.). After launch validation will be continued by collecting ground reflectance data for similar large and well characterized surfaces.

13.5 Error Budget

Uncertainty in the calculation of surface reflectance arise from many different sources. These include uncertainties in absolute calibration, aerosol optical depth retrieval, bidirectional effects, adjacency effects, and look-up table interpolations. Incorrect estimations of the aerosol optical thickness can result in significant errors in the surface reflectance calculation. In Figure 13-4, for example, it can be seen that for a TOA reflectance of 0.5, an error of 0.1 in aerosol optical depth results in a 0.01 error in surface reflectance. This error of course will be larger for higher surface reflectances, but in general most terrestrial surfaces are relatively dark. Man-made materials on the other hand, such as metals, paints, etc., can have very high reflectances.

The Lambertian surface reflection approximation may be the largest source of error in the surface reflectance retrieval process. Lee and Kaufman (1986) quantified the error due to the Lambertian approximation based on radiative transfer simulations at 0.65 and 0.85 μm using surfaces types ranging from forest to savanna. Surface reflectance errors ranged from 0.02 - 0.06 for clear atmospheres to 0.03 - 0.11 for hazy atmospheres (with aerosol optical depth equal to 0.5). Currently our surface reflectance algorithm does not include bidirectional effects, but it is clear that it must be included in order to predict accurate surface reflectance values.

The adjacency effect can also be a source of error in scenes containing adjacent targets of contrasting brightness. The adjacency effect occurs where bright targets lie next to dark targets. In this case solar radiation reflected from the bright surface can be scattered in to the beam from the dark surface to the instrument. In these situations it may be possible to apply a correction to account for this effect, however further research is needed in this area.

13.6 Software Implementation Plan and Status

Software has been written in IDL to calculate aerosol optical depth from in-scene data. An interface has been created to build comprehensive look up tables from multiple runs of the 6S atmospheric code. A third routine has been written to correct MTI TOA measurements to surface reflectance.

References

Fallah-Adl, H., J. Jaja, and S. Liang 1997, "Fast algorithms for estimating aerosol optical depth and correcting thematic mapper imagery," *J. Supercomputing*, **10**, pp. 315-329.

Fraser, R., R. Ferrare, Y. Kaufman, B. Markham, and S. Mattoo 1992, "Algorithm for atmospheric correction of aircraft and satellitd imagery," *Int. J. Remote Sensing*, **13**, 541-557.

Holben, B., E. Vermote, Y. Kaufman, D. Tanré, and V. Kalb 1992, "Aerosol retrieval over land from AVHRR data — Application for atmospheric correction," *IEEE Trans. Geosci. Rem. Sens.*, **30**, 212-220.

Holben, B.N., T. Eck, I. Slutsker, D. Tanre, J. Buis, A. Setzer, E. Vermote, J. Reagan, Y. Kaufman, T. Nakajima, F. Lavenu, I. Jankowiak, "Multiband Automatic Sun and Sky Scanning Radiometer System for Measurement of Aerosols," *Rem. Sens. Environ.*, In Press, 1998.

Kaufman, Y. and D. Tanré 1996, "Strategy for ddirect and indirect methods for correcting the aerosol effect on remote sensing," *Rem. Sens. Environ.*, **55**, 65-79.

Liang, S., H. Fallah-Adl, S. Kalluri, J. Jaja, Y. Kaufman, and J. Townshend 1997, "An operational atmospheric correction algorithm for Landsat Thematic Mapper imagery over the land," *J. Geophys. Res.*, **102**, 17173-17186.

Lee, T. and Y. Kaufman, "Non-Lambertian Effects on Remote Sensing of Surface Reflectance and vegetation Index," *IEEE Trans. Geosci. and Rem. Sens.*, Vol. 24, pp. 699 - 708, 1986.

Tanré, D. et al, 1996: "Description of a Computer Code to Simulate the Satellite Signal in the Solar Spectrum: 5S Code," *Int. J. Remote Sens.*, **11**, 659 - 668.

Teillet, P, and G. Fedosejevs, 1995: "On the Dark Target Approach to Atmospheric Correction of Remotely Sensed Data," *Canadian J. of Rem. Sensing*, **21**, 374 - 387.

Vermote, E., D. Tanre, L. Deuze, M. Herman, and J. Morcette, "Second Simulation of the Satellite Signal in the Solar Spectrum: An Overview," *IEEE Trans. Geosci. Rem. Sens.*, **35**, 675 - 686, 1997.

14. COLUMNAR WATER VAPOR RETRIEVAL

Christoph C. Borel and William B. Clodius

14.1 Introduction and Goal

The goal of this retrieval is to directly assay the column of water vapor between the satellite and the reflective ground surface. The light source is reflected sunlight. In the daytime MTI will be capable of making water vapor maps with 20 m GSD.

An atmospheric code (6S) and 562 spectra were used to compute the top of the atmosphere radiance near the 940 nm water vapor absorption feature in steps of 2.5 nm as a function of precipitable water (PW). We derive a novel technique called "Atmospheric Pre-corrected Differential Absorption" (APDA) and show that APDA performs better than the traditional "Continuum Interpolated Band Ratio" (CIBR) over many surface types.

14.2 Scientific Basis

Two different approaches exist to retrieve columnar water vapor from imaging spectrometer data:

1. Differential absorption techniques based on:

   (a) Narrow-Wide (N/W) ratio between overlapping spectrally wide and narrow channels (Frouin *et al.*, 1990).

   (b) Continuum Interpolated Band Ratio (CIBR) between a measurement channel and the weighted sum of two reference channels. (Green *et al.*, 1989, Bruegge *et al.*, 1990, Gao and Goetz, 1990a, and Carrére and Conel, 1993)

2. Non-linear fitting techniques which are based on spectral radiative transfer calculations (Gao and Goetz, 1990b, Green *et al.*, 1993).

The advantage of the first approach is computational speed and of the second, improved retrieval accuracy. Our goal was to improve the accuracy of the first technique using physics based on radiative transfer. Using a modified version of the Duntley equation (Middleton, 1952, p.68) we derived an "Atmospheric Pre-corrected Differential Absorption" (APDA) technique and described an iterative scheme to retrieve water vapor on a pixel-by-pixel basis. Next we compared both, the CIBR and the APDA using the Duntley equation for MODTRAN3 computed irradiances, transmissions and path radiance (using the DISORT option). This simulation showed that the CIBR

is very sensitive to reflectance effects and that the APDA performs much better. An extensive data set was created with the radiative transfer code 6S (Vermote *et al.*, 1994) over 562 different ground reflectance spectra. The calculated relative water vapor error was reduced significantly for the APDA. In the AVIRIS case APDA technique had about 6.2% (vs. 14% for the CIBR) of the 562 spectra with a relative water vapor error of greater than ±10%. The APDA has been applied to 1991 and 1995 AVIRIS scenes which visually demonstrate the improvement over the CIBR technique (see Schläpfer *et al.*, 1996).

14.3 Algorithm Steps

14. 3. 1 Derivation of the Atmospheric Pre-Corrected Differential Absorption Technique

Duntley in 1948 expressed the radiance L measured in channel i by a sensor as:

$$L_i = \rho_{g,i} \frac{E_i}{\pi} T_i + L_{h,i}\left(1 - T_i^*\right) = L_{g,i} T_{0,i} T_{w,i}(PW) + L_{p,i}(PW), \tag{14-1}$$

where $\rho_{g,i}$ is the ground reflectance, E_i is the solar irradiance, $T_{w,i}=T_{0,i}T_{w,i}(PW)$ is the total transmission and $L_{h,i}$ is the radiance one would measure in a plane parallel atmosphere in horizontal direction and T^*w,i is a special transmission term (Duntley assumes: $T_{w,i}= T^*_{w,i}$). The atmospheric transmission due to water vapor PW in [g/cm^2] is $Tw,i(PW)$. The transmission without any water vapor is $T_{0,i}$ and depends on aerosols and gas absorptions. To simplify the notation we define: $L_{g,i}=\rho_{g,i}\ E/\pi$. The path radiance $L_{p,i}$ is the sum of the atmospheric scattered radiance L_{atm} and the adjacency scattered radiance L_{adj}. Using this equation we first write the radiances in three channels i = {m, $r1$, $r2$} where m is a measurement channel in an absorption region, e.g. the 940 nm water vapor absorption, and $r1$ and $r2$ are two reference channels. The transmission $T_{w,i}(PW)$ is a function of water vapor for channel m but not for the reference channels $r1$ and $r2$. Assuming a small difference between the central wavelengths λ_{r1} and λ_{r2} of the reference channels and $\lambda_r < \lambda_m\} < \lambda_{r2}$ the radiance $L_m(PW)$ can be approximated by a linear interpolation as:

$$L_m = [w_{r1}\, L_{g,r1}\, T_{0,r1} + w_{r2}\, L_{g,r2}\, T_{0,r2}] T_m(PW) + L_{p,m}(PW), \tag{14-2}$$

where

$$w_{r1} = \frac{\lambda_{r2} - \lambda_m}{\lambda_{r2} - \lambda_{r1}} \text{ and } w_{r2} = \frac{\lambda_m - \lambda_{r1}}{\lambda_{r2} - \lambda_{r1}}.$$

Note that we assume the reference channels have no water vapor absorption or $T_{r1}(PW) = 1$ and $T_{r2}(PW) = 1$. Solving equation (14-2) for the transmission in the water vapor channel $T_m(PW)$ and

substituting $L_{g,r1}$ and $L_{g,r2}$ from equation (14-1) we find an equation similar to the CIBR, but with atmospheric pre-correction terms for the path radiances $L_{p,i}$:

$$T_m(PW) = \frac{L_m - L_{p,m}(PW)}{w_{r1}(L_{r1} - L_{p,r1}) + w_{r2}(L_{r2} - L_{p,r2})} \tag{14-3}$$

Note, however that $L_{p,m}$ is also a function of water vapor which can be expressed using a polynomial of second (or higher) order:

$$L_{p,m}(PW) = aPW^2 + bPW + c + L_{adj,m}, \tag{14-4}$$

where we neglect the adjacency path radiance $L_{adj,m}$ for now. In future work we plan to incorporate the adjacency effect in the retrieval over small dark targets and shadow regions where the adjacency effect dominates. The polynomial coefficients *a, b,* and c are fitted to the total radiance over a zero ground reflectance computed by a radiative transfer code such as MODTRAN3 (Abreu *et al.*, 1995) or 6S for the given observation geometry and assumed atmospheric conditions. Thus

$$R_{APDA}(PW) = \frac{L_m - (aPW^2 + bPW + c)}{w_{r1}(L_{r1} - L_{p,r1}) + w_{r2}(L_{r2} - L_{p,r2})}. \tag{14-5}$$

14. 3. 2 Iterative retrieval of water vapor

The following iterative procedure, shown in Figures 14-1 and 14-2, can be used to compute the water vapor $PW(j,k)$ for pixel (j,k):

1. Use a radiative transfer code (6S or MODTRAN 3) to compute the path radiance $L_{p,m}$ for an average reflectance background (e.g. $\rho_{g,i} = 0.4$) as a function of water content and fit a polynomial (eq.(14-4)) to $L_{p,r1}$ and $L_{p,r2}$ for a zero reflectance background. Note that the path radiances $L_{p,r1}$ and $L_{p,r2}$ are assumed to be independent of *PW*.

2. Use a spectral radiative transfer code (6S or MODTRAN 3) to compute the total radiance over a zero reflectance background as a function of water vapor *PW*. Because the ratio $R_{APDA}(PW)$ decreases smoothly with increasing water vapor a spline interpolation is used to go from a given ratio to columnar water vapor.

3. Assume as a starting value an average water vapor $\overline{PW}_1$ for the whole scene.

4. Estimate R_{APDA} (j,k) for each pixel (j,k) using equation (14-5) and use the cubic spline interpolation to get a second estimate $PW_2(j,k)$ for the columnar water vapor.

5. Substitute $PW_2(j,k)$ for PW the right side of equation (14-5) to get a better ratio R_{APDA} (j,k).

6. Determine from the second ratio R_{APDA} (j,k) a third water vapor amount $PW_3(j,k)$ using the cubic spline interpolation.

7. Repeat steps 5 and 6 a fixed number of times or until $|PW_i(j,k) - PW_{i-1}(j,k)| < 10^{-4}$.

We have compared this iterative technique with the optimum solution where we assume the water vapor is known exactly. The iterative solution performs within 0.5% of the optimal solution for the 6S generated data set.

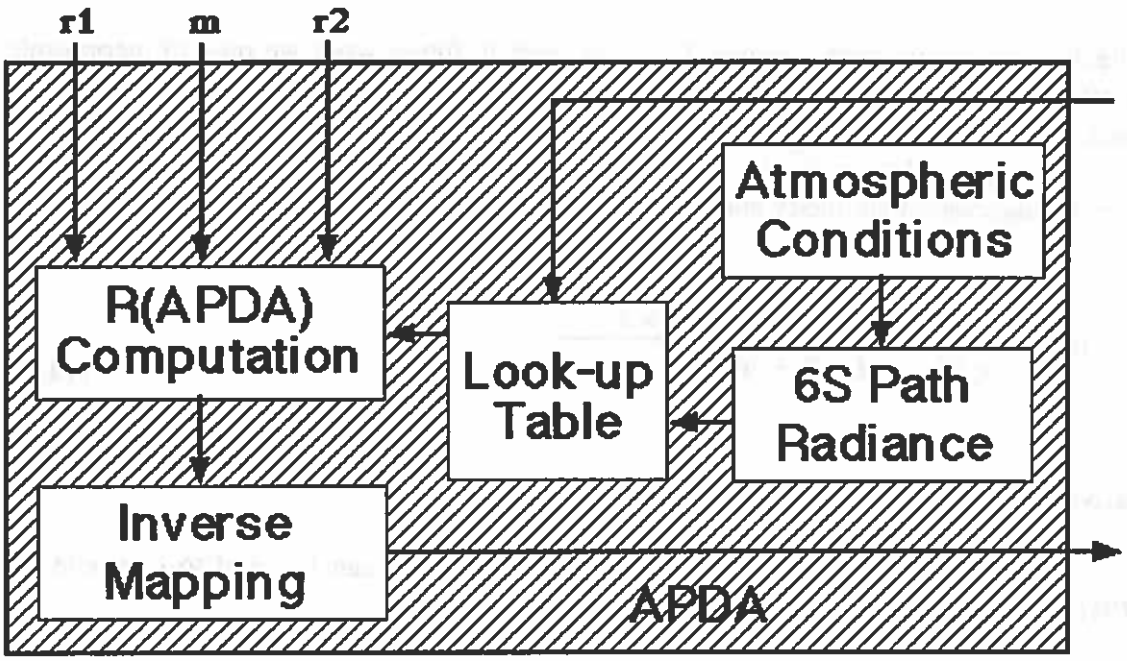

Figure 14-1: Flow diagram for non-iterative APDA algorithm.

14.4 Error Budget

A detailed error budget is published in Borel et al (1996) for many surface backgrounds. The MTI bands are: $E = r1$: 0.86-0.89 μm; $F = m$: 0.91-0.97 μm; and $G = r2$: 0.99-1.04 μm.

If we compare the retrieval methods by setting thresholds at ±5% and ±10% RMS relative water vapor and counting the number of spectra which indicate how robust the retrievals are over many different backgrounds. Table 14-1 summarizes the results obtained for all 562 background spectra using the four above described techniques:

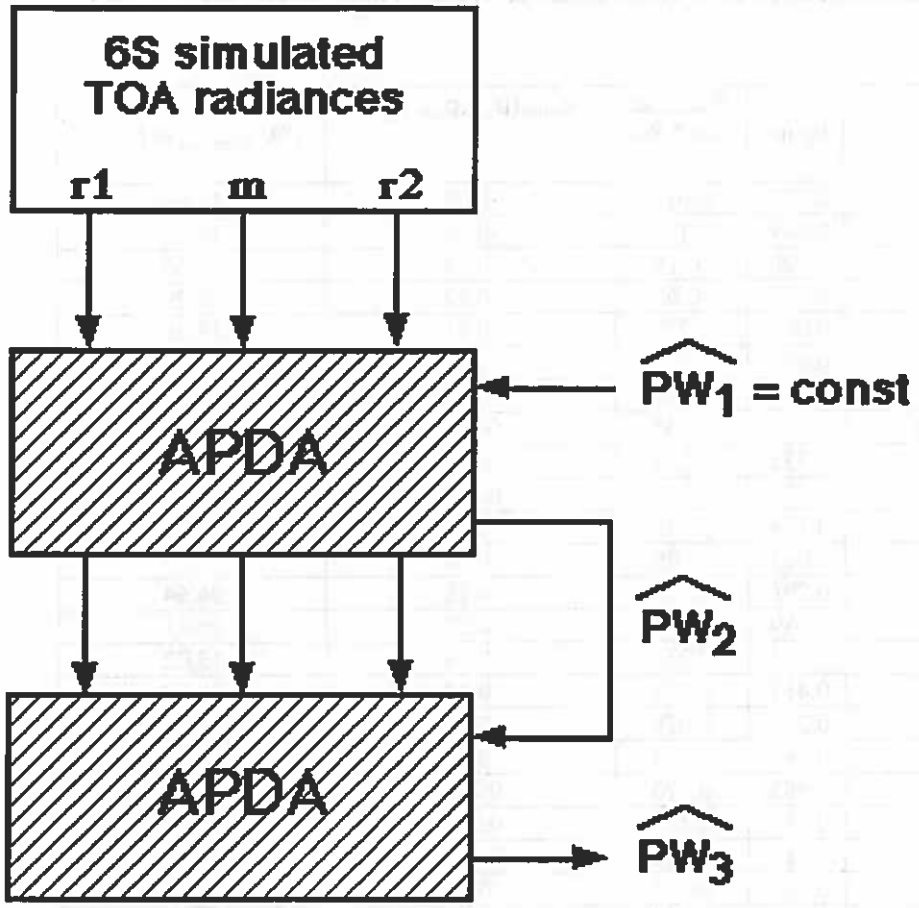

Figure 14-2: Iterative APDA algorithm, in which each instance of the basic APDA contains the scheme in Fig. 14-1.

Table 14-1: Percentage of Materials above 5% and 10% RMS Relative Water Vapor Error

Retrieval Method	Multispectral 5%	Multispectral 10%
CIBR	32.6	15.6
APDA	22.4	5.7
APDA(optimal)	22.9	5.7
APDA(iterative)	21.7	5.7

Specific materials with a water vapor error of greater than 10% are listed in Table 14-2.

Table 14-2: Percentage of Materials above 10% RMS Relative Water Vapor Error (MTI Case)

Mineral Name	Þg,m	$\frac{\rho_{g,r2} - \rho_{g,r1}}{\rho_{g,r2} + \rho_{g,r1}}$	$R_{CIBR}(\rho_{g,r1},\rho_{g,m},\rho_{g,r2})$	$PW_{rel.err.,iter}$ in [%]
ANTHOPHYLLITE-IN-8A	0.559	0.013	-0.06	12.64
ANTLERITE-SO-11A	0.149	0.125	-0.10	14.22
Augite	0.290	-0.19	-0.02	10.63
Axinite	0.173	-0.65	-0.22	86.29
Azurite	0.065	0.238	-0.11	13.26
Beryl	0.671	0.204	0.020	-16.8
Bronzite	0.134	0.262	-0.29	62.32
BUDDINGTONITE-NHB2301	0.550	0.035	0.004	-11.2
Copiapite	0.332	0.211	-0.09	10.74
Cuprite	0.157	0.115	0.021	-12.3
CUMMINGTONITE-IN-6A	0.128	-0.05	-0.09	21.56
DICKITE-PS-3A	0.055	-0.05	-0.08	16.73
ENSTATITE-IN-10B	0.295	0.159	-0.18	36.64
FAYALITE-NS-1A	0.089	-0.18	-0.07	20.61
HEMATITE-FE2602	0.231	0.236	-0.14	15.02
Hypersthene	0.415	0.121	-0.14	29.28
Jarosite	0.283	0.078	-0.10	16.97
Lepidocrosite	0.245	0.009	-0.08	16.17
Monazite	0.483	0.170	0.135	-41.4
MOLYBDENITE-S-11A	0.254	0.191	0.025	-16.3
Neodymium Oxide	0.917	0.201	0.144	-48.2
Samarium Oxide	0.797	-0.03	-0.11	23.24
Siderite	0.113	-0.20	-0.05	19.34
Sphalerite	0.466	0.169	0.003	-10.6
SIDERITE-COS2002	0.204	-0.24	-0.05	15.01
TOURMALINE-DRAVITE-S-CS-1A	0.083	-0.10	0.075	-12.3
TRIPHYLITE-P-4A	0.440	-0.30	-0.02	18.89
Tephroite	0.138	-0.07	-0.06	14.93

14.5 Validation Plan

Validation of the retrieval algorithm will require several of concurrent measurements such as:

- Con-temporal radio-sonde measurements of relative humidity, temperature and pressure profiles.
- Simultaneous ground based sun-photometer measurement of optical depth.
- Uniform ground coverage with 10 nm sampling reflectance spectrum.
- Good cross-calibration of channels E, F and G with an airborne imaging spectrometer (e.g. AVIRIS).

14.6 Software Implementation Concept

Software exists to evaluate water vapor for AVIRIS cubes. With some necessary adjustments for the look-up table generation using MODTRAN it should be possible to have an operational APDA algorithm ready very soon.

References

Abreu L.W., Chetwynd J.H, Anderson G.P. and Kimball L.M., 1995: "MODTRAN 3 Scientific Report," Draft Preprint, Geophysics Laboratory, Air Force Command, US Air Force, Hanscom AFB, MA, USA.

Borel, C.C, and Schläpfer, D., 1996: "Atmospheric Pre-Corrected Differential Absorption Techniques To Retrieve Columnar Water Vapor: Theory," *Proceedings of the 6th JPL Airborne Earth Science Workshop*, JPL, Pasadena.

Bruegge, C.J., Conel, J.E., Margolis, J.S., Green, R.O., Toon, G., Carrére, V., Holm, R.G., and Hoover, G., 1990: "In-situ Atmospheric Water-Vapor Retrieval in Support of AVIRIS Validation.," *SPIE Vol. 1298 Imaging Spectroscopy of the Terrestrial Environment*, pp 150 - 163.

Carrére, V., and Conel, J. E., 1993: "Recovery of Atmospheric Water Vapor Total Column Abundance from Imaging Spectrometer Data around 940 nm - Sensitivity Analysis and Application to Airborne Visible/Infrared Imaging Spectrometer (AVIRIS) Data," *Remote Sensing of Environment*, Nr. 44 , pp 179 - 204.

Clark, R.N., Swayze, G.A., Gallagher, A.J., King, T.V.V., and Calvin, W.M., 1993, U.S. Geological Survey, Open File Report 93-592 or anonymous FTP: speclab.cr.usgs.gov or e-mail to rclark@speclab.cr.usgs.gov.

Frouin, R., Deschamps, P.-Y., and Lecomte, P., 1990: "Determination from Space of Atmospheric Total Water Vapor Amounts by Differential Absorption Near 940 nm: Theory and Airborne Verification," *Journal of Applied Meteorology*, **29**, American Meteorological Society, pp. 448 - 459.

Gao, B.-C., and Goetz, A.F.H., 1990a: "Determination of Total Column Water Vapor in the Atmosphere At High Spatial Resolution from AVIRIS Data Using Spectral Curve Fitting and Band Ratioing Techniques," *Imaging Spectroscopy of the Terrestrial Environment, Proc. SPIE*, **1298**, pp 138 - 149.

Gao, B.-C., and Goetz, A.F.H., 1990b: "Column Atmospheric Water Vapor and Vegetation Liquid Water Retrievals from Airborne Imaging Spectrometer Data," *Journal of Geophysical Research*, **95**, pp 3549 - 3564.

Green, R.O., Carrére, V., and Conel, J.E., 1989: "Measurement of Atmospheric Water Vapor Using the Airborne Visible/Infrared Imaging Spectrometer," Am. Soc. Photogram. and Remote Sensing Proc., Workshop on Image Processing, Sparkes, Nevada, 23-26 May.

Middleton, W.E.K., 1952: *Vision Through the Atmosphere*, University of Toronto Press.

Schläpfer, D., Borel, C.C., Keller, J., and Itten, K., 1996: "Atmospheric Pre-Corrected Differential Absorption Techniques to Retrieve Columnar Water Vapor: Application to AVIRIS 91/95 Data," *Proceedings of the 6th JPL Airborne Earth Science Workshop*, JPL, Pasadena.

Vermote, E., Tanré, D., Deuzé, J.L., Herman, M., and Morcette, J.J., 1994: "Second Simulation of the Satellite Signal in the Solar Spectrum. — 6S User Guide Version 0," NASA-Goddard Space Flight Center, Greenbelt , USA, p 182.

15. VEGETATION ANALYSIS

Pierre V. Villeneuve and Christoph C. Borel

15.1 Algorithm Objective

Remote sensing of vegetation is important to the MTI community for various reasons. From a science point of view MTI offers an opportunity to make measurements of vegetation canopies at spatial scales not readily available from other space-born instruments. From a nonproliferation point of view, analysis of the vegetation surrounding a facility of interest can provide ancillary information useful in the evaluation of a facility's operation.

This chapter defines the data products related to vegetation analysis in MTI scenes. These data products include the normalized difference vegetation index (Level 2 - NDVI) and the vegetation health product (Level 4 - Veg).

15.2 Scientific Basis

15.2.1 Normalized Difference Vegetation Index

Many studies have shown how red and near-infrared (NIR) reflected energy are related to the amount of vegetation present on the ground (Colwell, 1974). Reflected red energy decreases with plant development due to chlorophyll absorption in an actively photosynthetic plant. Reflected NIR energy, on the other hand, will increase with plant development as most of this energy is reflected and transmitted with very little absorbed in healthy leaves. Unfortunately, because the amount of radiation reflected from a plant canopy and reaching a satellite sensor varies with solar irradiance, atmospheric conditions, non-photosynthetic vegetation (NPV), canopy background, and canopy structure/composition, a simple measure of light is not sufficient to quantify plant biophysical parameters. Individual band data are thus not appropriate for vegetation studies due to the intricate radiant transfer processes at both the leaf level (cell constituents, leaf morphology) and canopy level (leaf elements, orientation, NPV, and background). This problem has been circumvented somewhat by combining two or more bands into an equation or "vegetation index" (VI).

Deering (1978) developed the modern form of the nondimensional vegetation index (NDVI) as the ratio of the difference between NIR and red measurements to the sum of the NIR and red:

$$NDVI = (\rho_{NIR} - \rho_{red})/(\rho_{NIR} + \rho_{red})$$

where X can be digital counts, top of the atmosphere radiance, surface reflectance, etc. NDVI theoretically ranges from -1 to +1, however for terrestrial targets the lower boundary is typically zero for conditions of no vegetation.

The NDVI is a very robust and sensitive vegetation measure, utilizing the spectral contrast in vegetation canopy reflected energy in the red and near-infrared portions of the electromagnetic spectrum. It is currently the only operational, global-based vegetation index utilized. This is in part due to its "ratioing" properties, which enable the NDVI to cancel out a large proportion of signal variations attributed to changing irradiance conditions that accompany changing sun angles, topography, clouds/shadow and atmospheric conditions.

Many studies have shown that NDVI is related to leaf area index (LAI), green biomass, and other biophysical parameters. One problem in relating NDVI to parameters such as LAI which quantify the amount of vegetation is that NDVI quickly saturates after the canopy becomes optically thick. In this situation the NDVI is only a measure of the top-most levels of the canopy. Other potential limitations on the use of NDVI include nonlinearities between NDVI and biophysical parameters, ground litter contamination, and canopy structural effects. Atmospheric transmission and path radiance effects will be minimal with the MTI NDVI product since this algorithm will use as input the atmospherically corrected surface reflectance (Level 2 - Refl).

15.2.2 Vegetation Health

Vegetation stress caused by human activity is of interest to the MTI comunity from a nonproliferation point of view since it can be related to the environmentally unfriendly activities of a nearby processing plant or facility. For this reason we would ideally like to differentiate between naturally-stressed vegetation from anthropogenically-stressed vegetation. This is not possible from a passive remote sensing aspect since there does not exist a direct correlation between a source of stress and the plant's measured stress response. We must therefore settle for the identification of plant stress regardless of it's cause. The MTI vegetation health data product is classified as a Level 4 product. The reason for this is that the data product will not be produced automatically for each scene, and that a considerable amount of human interaction will be required to produce this result. For example, in order to produce a map of stressed vegetation, it may be necesary for a technician to evaluate a number of MTI data products (NDVI, land surface temperature, columnar water vapor, etc.) and to consult with outside sources of information such as the past history of the regional weather.

Stress may be defined as an environmental factor potentially unfavorable to living organism (Levitt, 1980). Thus, for plants, stress is a state in which increasing demands made upon the plant lead to an initial destabilization of functions, followed by normalization and then improved resistance. If the limits of tolerance are exceeded and the adaptive capacity of the plant is overworked, the result may be permanent damage or even death (Larcher, 1987). The stress threshold is exceeded when the plant can no longer compensate for the physiological change cause by the stress. When this threshold of stress resistance has been passed, the result is often permanent damage. A short-term high level stress can in principal induce the same damage as a long-term low level stress.

Natural sources of stress include water shortage, insects, nitrogen shortage, heat, cold, etc. Examples of anthropogenic sources of plant stress include herbicides, air pollutants (SO_2, NO, etc), acid rain, and high Ph levels in water and soil. The stress tolerance capacity of a plant species is genetically fixed and may be relatively high or low compared to the average regional plant type.

From a remote-sensing point of view, the only aspect of plant stress which can be measured is the manner in which the plant reacts to stress. These coping mechanisms (both chemical and architectural) will depend on the plant type and the type and degree of stress. For example, water stress will in general result in higher reflectances across the visible and SWIR spectral regions (Jackson and Ezra, 1985). This is illustrated in Figure 15-1 which shows leaf reflectance and transmittance for varying degrees of leaf water stress. Water stress response is further complicated by the fact that water stress will also cause a change in plant architecture by causing the leaves to droop, which in turn can affect the canopy bidirectional reflectance properties.

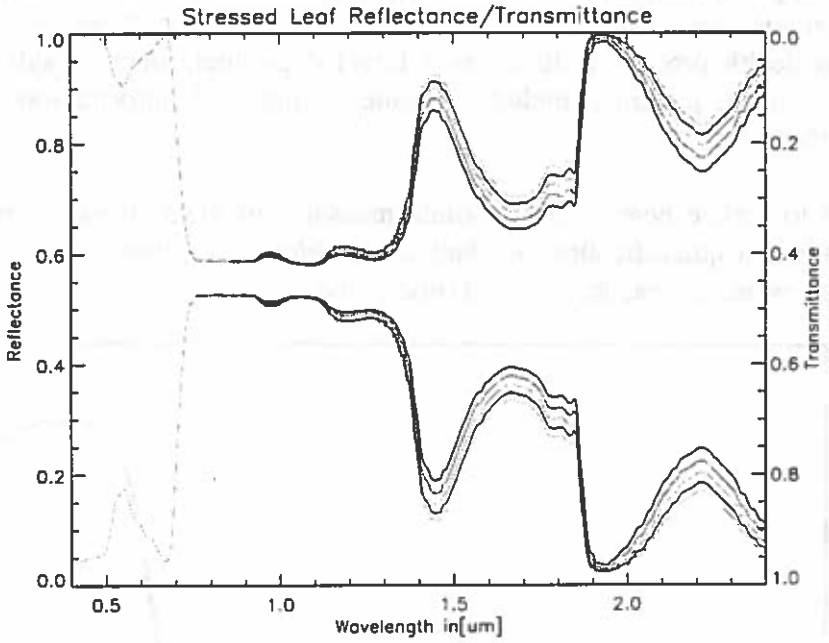

Figure 15-1. Leaf reflectance and transmittance versus wavelength for various levels of water stress.

Other sources of stress will result in different plant responses. Increasing levels of air pollution can affect the concentrations of photosynthetically active leaf pigments which can be measured to some degree in the visible spectrum (Gitelson, et al., 1996). Analysis of TMS data (Vogelmann and Rock, 1986) has shown a correlation between ratios of radiances 1.65 µm/0.83 µm and 1.65 µm/1.23 µm with damage in coniferous forests thought to be caused by increases in air pollution. This correlation may also be confused by a decrease in canopy density, which in turn increases the exposure of the soil and undergrowth which have higher reflectances at 1.65 µm.

In a past study (Borel, 1996) we generated simulated canopy reflectance data using the radiosity method, the PROSPECT leaf chemistry model (Jacquemoud and Baret, 1990) and soil data from

SOILSPEC (Jacquemoud, 1992). This allowed us to vary leaf area index and leaf chemistry (water, chlorophyll content) and leaf structure over a range of scene conditions. It was found that the area under the visible spectrum chlorophyll peak was strongly correlated with leaf chlorophyll amount. The area calculation is illustrated in Figure 15-2 for a typical plant visible/NIR spectrum with reflectance measurements made at blue, green, and red wavelengths (MTI bands A, B and C). The model calculations of the chlorophyll peak area versus leaf chlorophyll amount are shown in Figure 15-3 along with a calculated signal to noise ratio. Attempts to measure leaf chlorophyll amount using this technique will of course be complicated by mixed pixels, underlying bare soil and ground litter for sparse canopies. Use of algorithms of this type to predict relative chlorophyll amounts within a scene will be useful in characterizing vegetation state of health.

Clearly a large amount of research has been reported in the literature on the estimation of plant stress from visible/NIR passive remote sensing measurements. However there has not yet been developed a widely applicable algorithm to positively differentiate stressed vegetation pixels from healthy vegetation pixels over a range of climate conditions. It is in part because of this fact that the MTI vegetation health product is listed as a Level 4 product, since it will require human intervention to recognize patterns, include outside sources of information, and to make assumptions about the scene.

An important point to realize here is that absolute measures of plant stress are meaningless. A more useful measure is a quantification of plant stress *relative* to what is expected for a given regional climate, past weather, season, soil, and time of day.

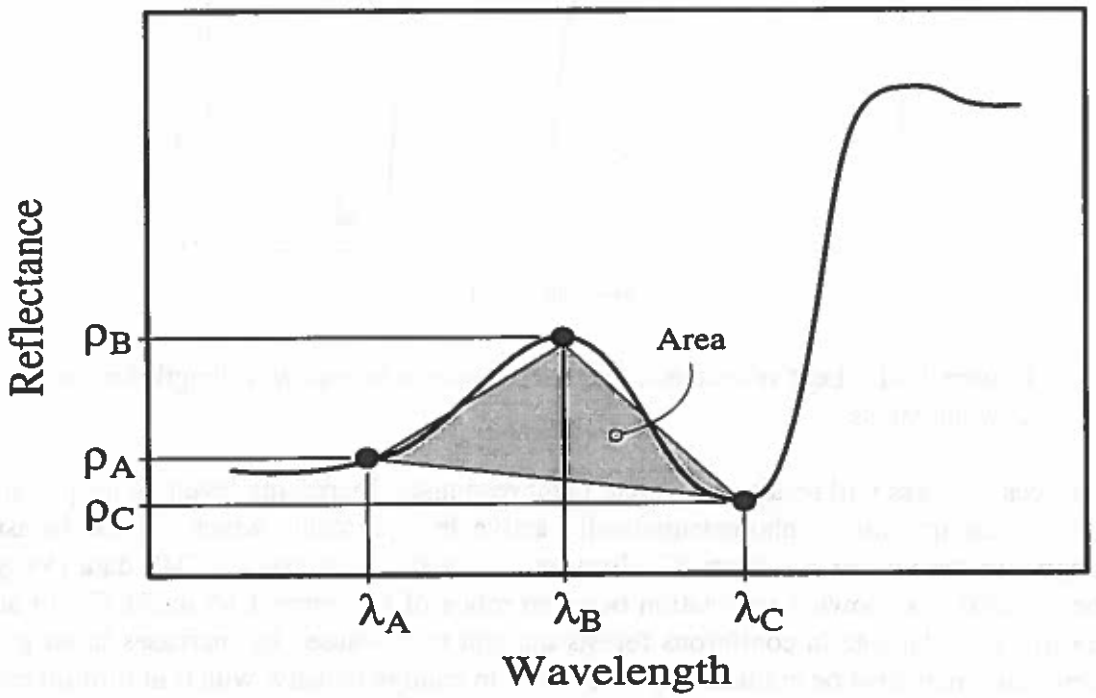

Figure 15-2. Chlorophyll green peak area calculated from three spectral reflectance measurements.

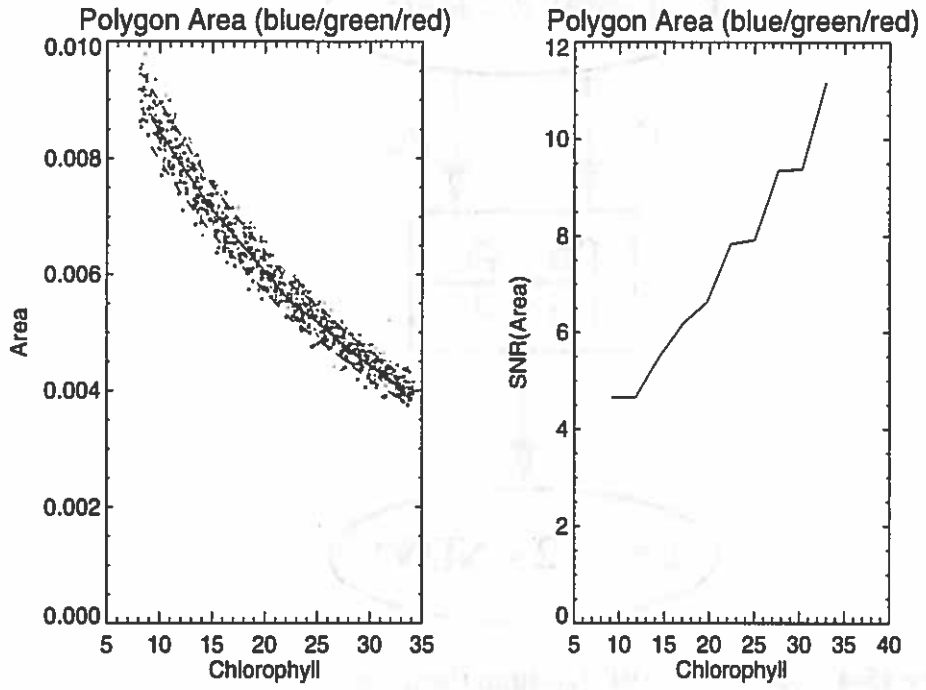

Figure 15-3. Scatter plot of the grean peak area and SNR versus chlorophyll concentration.

15.3 Algorithm Steps

15.3.1 Normalized Difference Vegetation Index Algorithm

The algorithm to calculate NDVI is quite simple and is illustrated in Figure 15-4. It is simply the contrast across the so-called "red edge" reflectances normalized by the sum of the red and NIR reflectances. This product can only be calculated for daytime measurements because of it's dependence on the solar spectrum. The surfaces reflectances from Level 2 - Refl are used instead of the TOA radiances in an effort to reduce the effect of atmospheric path radiance. Many modified versions of NDVI are found in the literature which have been developed to include intrinsic atmospheric corrections when applied to TOA radiances. These modified types of NDVI algorithms are most often used in cases when atmosperic corrections have not been applied to the sensor data.

15.3.2 Vegetation Health Map

An automated unsupervised algorithm will not be implemented for the calculation of the Vegetation Health Map (Level 4 - Veg). This is because there is no direct and independent correlation between sources of stress, plant physiological reaction to stress, and leaf spectral reflectance. Therefore additional sources of information and further scene analysis is required before an acceptable health map can be created. The exact procedures to determine stressed

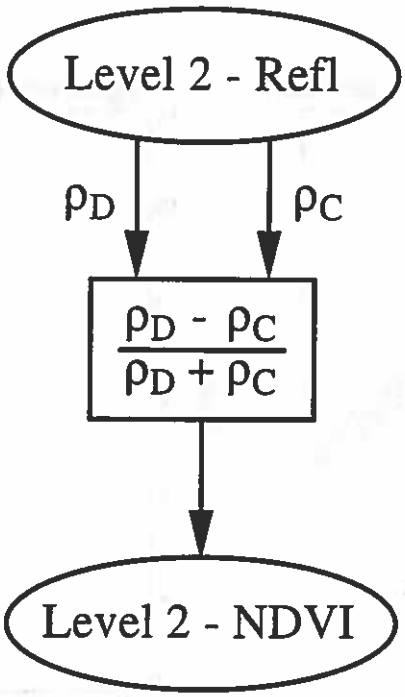

Figure 15-4. Level 2 - NDVI algorithm flowchart.

vegetation and the nature of ancillary sources of information are yet to be defined. A conceptual flowchart for this algorithm is shown in Figure 15-5.

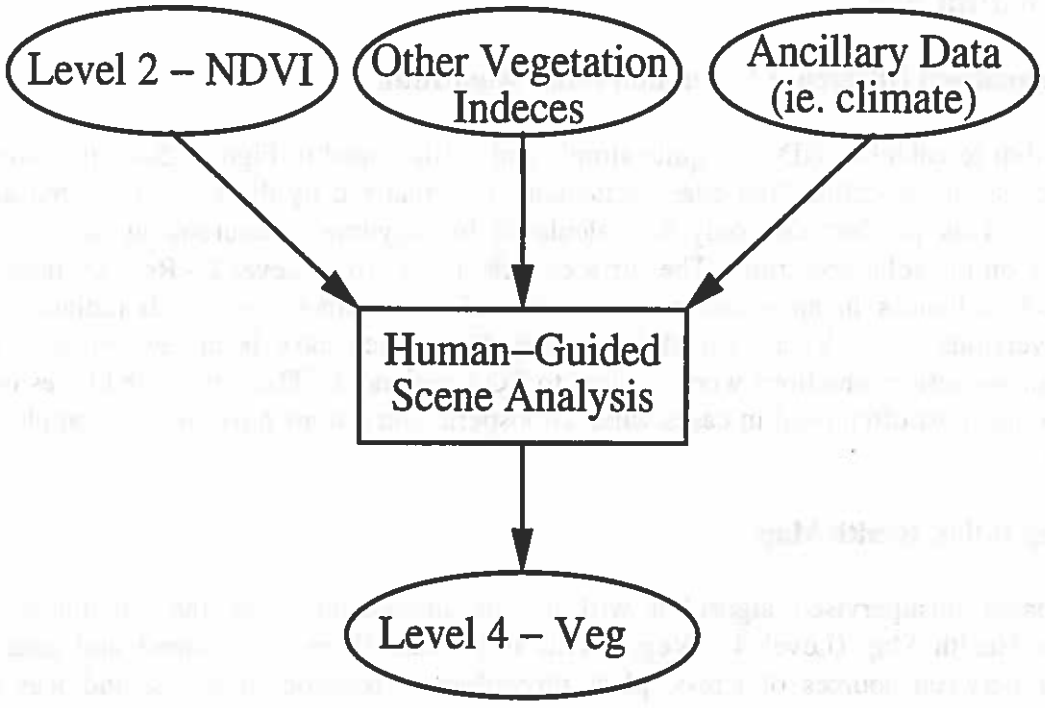

Figure 15-5. Level 4 - Veg conceptual algorithm flowchart.

15.4 Validation Plan

The validation processes for the two algorithms discussed in this chapter are inherently closely related. The most effective validation of the NDVI product will be a vicarious calibration comparing MTI NDVI data with coregistered and near co-temporal ASTER NDVI data. Because of the differences in the relatives orbits of the MTI spacecraft and EOS AM-1 (upon which ASTER resides), there will be numerous occasions for viewing the same earth scene within a few minutes of each other. The only complicating factor is that the viewing angles will most likely not be the same, meaning that a bidirectional reflectance correction will be required before the two data sets can be compared. Validation will entail comparing the two sets of NDVI value after they have been coregistered together. A further complication is that ASTER has a 15-m pixel size where MTI has a 5-m pixel size (bands A - D only).

Validation of the vegetation health product will take place at several sites with known stressed vegetation. Savanah River Site (SRS) has a number of well documented target areas including waste sites, seepage basins, contaminated streams and recovering vegetation in formerly hot streams. These sites at SRS have been observed with ground-based and airborn instruments over a period of many years giving a well know history of vegetation health and signatures. Other sites of interest include the DOE ARM site in Oklahoma where a number of wheat fields with sections of high alkalinity have been found which show signs of vegetation stress. We will also take advantage of appropriate vegetation scenes observed as part of other MTI data product validation campaigns.

15.5 Error Budget

Sources of error in the NDVI are improper atmospheric correction in the Level 2 - Refl algorithm, mixed pixels, and background contamination by surface litter (dead leaves, branches, etc.). Sources of error in the determination of stressed vegetation are varied. Vegetation stress levels depend on a large number of factors which, in many cases, are impossible to determine from a multispectral passive remote sensing instrument. Further development and testing will be required before a qualitative number can be given for the accuracy with which MTI can detect stressed vegetation.

15.6 Software Status

The software for these two data products has not yet been developed. The procedure for NDVI is a very simple calculation involving the surface reflectance from two visible/NIR channels. The software for vegetation health can only be implemented after further research has been conducted with simulated MTI cubes synthesized from AVIRIS, MAS, and other similar instruments.

References

Borel, C. C., "Nonlinear spectral mixing theory to model multispectral signatures," *Proc. Eleventh Thematic Conference and Workshops on Applied Geologic Remote Sensing*, Las Vegas, NV, 27-29 Feb. 1996, pp. II-11 - II-20.

Colwell, J.E., "Vegetation Canopy Reflectance," *Remote Sens. Environ.*, Vol. 3, pp. 175 - 183, 1974.

Gisler, G., and C. C. Borel, "Neural network identifications of spectral signatures," *Proc. Eleventh Thematic Conference and Workshops on Applied Geologic Remote Sensing*, Las Vegas, NV, 27-29 Feb. 1996, pp. II-21-29.

Gitelson, A., Y. Kaufman, M. Merzlyak, "Use of a Green Channel in Remote Sensing of Global Vegetation from EOS-MODIS," *Remote Sensing of Environment*, Vol. 58, pp. 289 - 298, 1996.

Jackson and Ezra, 1985: "Spectral Response of Cotton to Suddenly Induced Water-Stress," *Int. J. Remote Sens.*, **6**, No. 1, pp. 177 - 185.

Jacquemoud, S., and F. Baret, "PROSPECT: A model of leaf optical properties spectra," *Remote Sensing of the Environment*, **34**, 75-91, 1990.

Jacquemoud, S., F.Baret and J.F. Hanocq, "Modeling spectral and bidirectional soil reflectance," *Remote Sensing of the Environment*, **41**, 123-132, 1992.

Larcher, 1987: "Stress in Plants," *Naturwissenschaften*, **74**, No. 4, pp. 158 - 167.

Levitt, 1980: *Responses Plants Env.*, **1**, 1980.

Vogelmann, J. E., and B. N. Rock, 1986: "Assessing Forest Decline in Coniferous Forests of Vermont Using NS-001 Thematic Mapper Simulator Data," *Int. J. Remote Sens.*, **7**, No. 10, pp. 1303 - 1321.

16. MATERIAL IDENTIFICATION

Pierre V. Villeneuve and Christoph C. Borel

16.1 Algorithm Objective

The purpose of this algorithm is to distinguish between various types of materials within an MTI scene solely from measurements in the visible and near infrared spectral regions. An important aspect of material identification is distinguishing man-made objects from natural objects. Most man-made objects are made of metals, plastics, concrete, etc. and have a unique spectral signature when compared to naturally occurring materials.

16.2 Scientific Basis

The MTI instrument measures solar-reflected and earth-emitted radiation in fifteen different wavelength regions. However, not all channels are appropriate for the material identification procedure, and in fact only nine of the fifteen are applicable. The other channels are sensitive to either high-altitude cirrus clouds or thermal emission. The nine channels are the visible and near-IR channels A-G, I and O.

The technique we have selected to identify materials from multispectral imagery is a k-means clustering algorithm. There are several variants of the k-means clustering algorithm, but most involve an iterative scheme which operates over a fixed number of clusters, while attempting to satisfy the following conditions: 1) Each cluster has a center which is the mean position of all samples in that cluster. 2) Each sample is a member of the cluster to whose center it is closest. The k-means algorithm has been found by many to be most efficient for addressing this type of problem (Al-Sultan, 1996).

The clustering process is typically started with an initial clustering of the data (which may be random), and then passes from sample to sample, assigning each to the nearest cluster. The cluster centers are recomputed after each data sample reassignment. Figure 16-1 shows an example of a data set before and after a k-means clustering algorithm has been applied. The initial condition for each point is a random assignment to one of the two clusters. After iterating through the algorithm several times, the resulting classification is two clearly identifiable clusters.

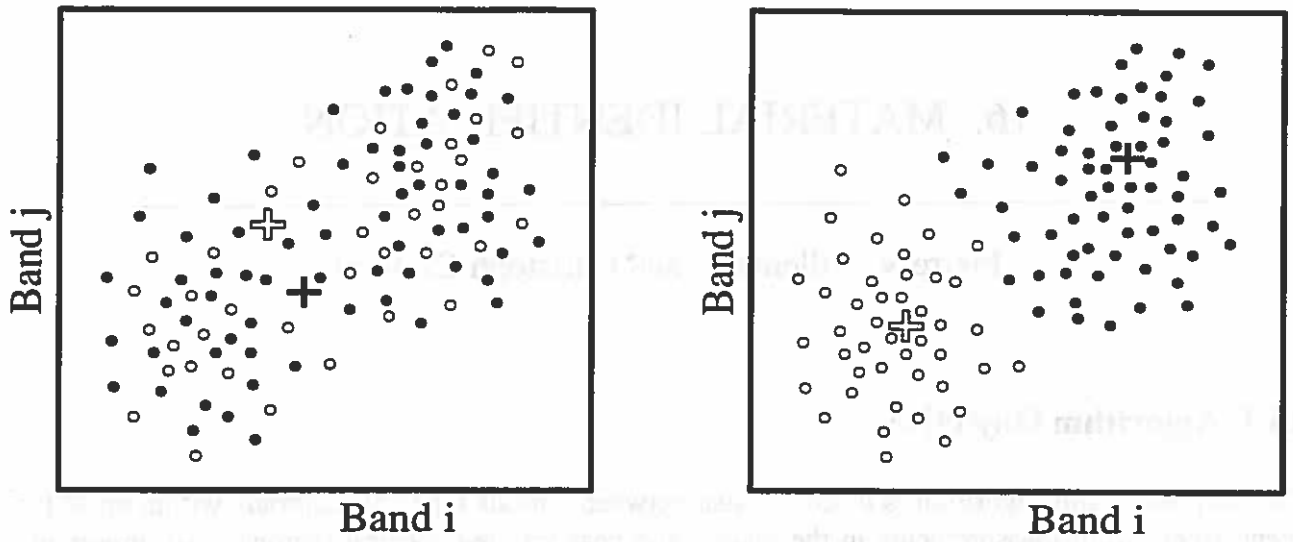

(a) Initial random clustering. (b) Clustered data.

Figure 16-1. Change in cluster centers as a result of k-means clustering.

The total number of clusters is not automatically calculated by the of algorithm and must be specified by the user. Therefore, the process of calculating the cluster centers should be supervised to iterate on the total number of clusters and some clusters may also be merged together when spectra are improperly assigned.

16.3 Algorithm Steps

Figure 16-2 shows a flow chart for the material identification algorithm. The inputs to this algorithm are the atmospherically corrected surface reflectance from the Level 2-Refl data product and a comprehensive spectral library of material signatures. Human assistance may be required to fine tune the subsetting of the spectral library to focus on a particular set of materials, depending on the nature of the target and the desires of the client.

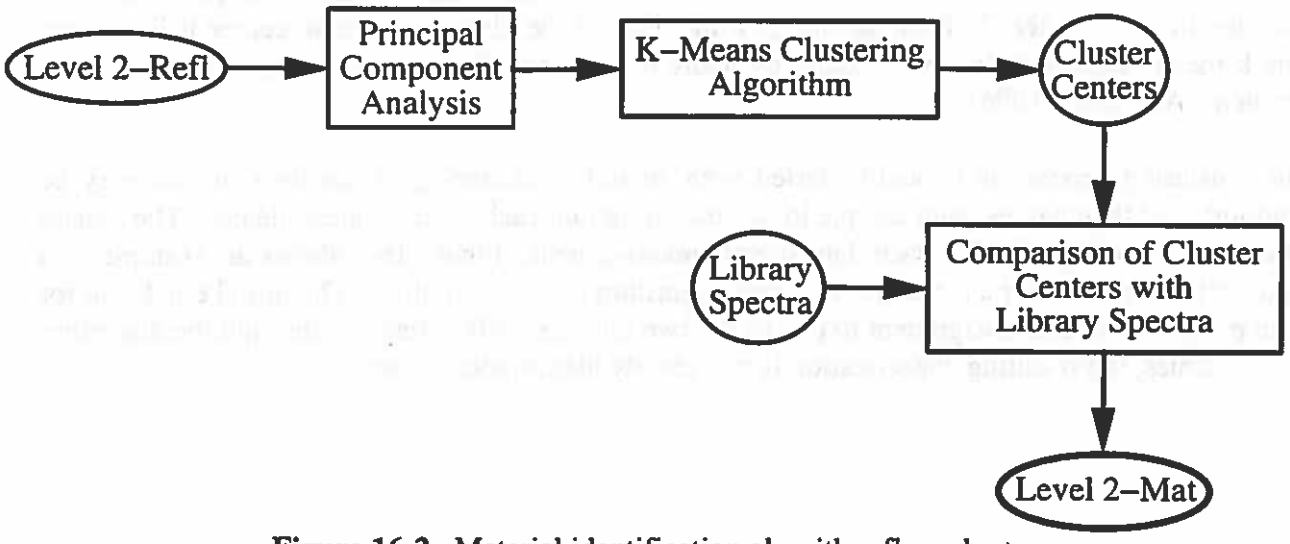

Figure 16-2. Material identification algorithm flow chart.

Four spectral libraries with a total of approximately five hundred spectra were used in the creation of our spectral database. These spectra were obtained in part from the NIST and the EPA spectral libraries. Examples of spectra from our combined library may be found in Figure 16-3. Through iteration it was found that twenty-two clusters was an optimum number of clusters for the combined spectral library data by applying the clustering algorithm to the spectral library itself (instead of the scene data). While these spectral libraries cover a wide range of wavelengths, only those regions associated with the above-mentioned nine MTI channels are considered. A principal component analysis was performed on our MTI spectral library. Figure 16-4 shows the eigenvalues corresponding to each principal component and Figure 16-5 shows the first four principal component vectors. The first PC is essentially constant with wavelength. The second PC is primarily a contrast between channel D and channels I and O. The third PC is a contrast between the visible channels and the near-infrared channels.

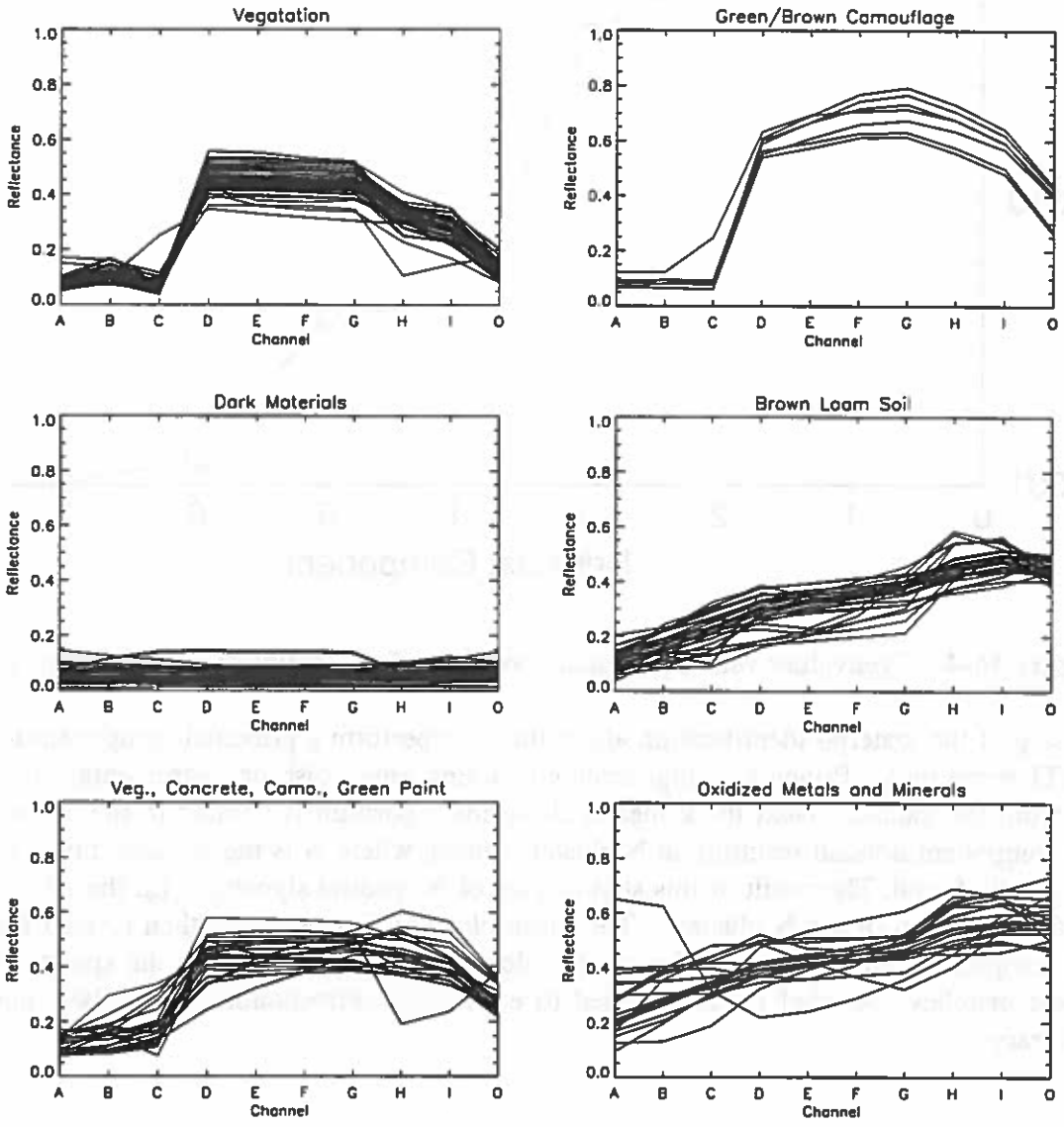

Figure 16-3. Example material signatures from spectral library.

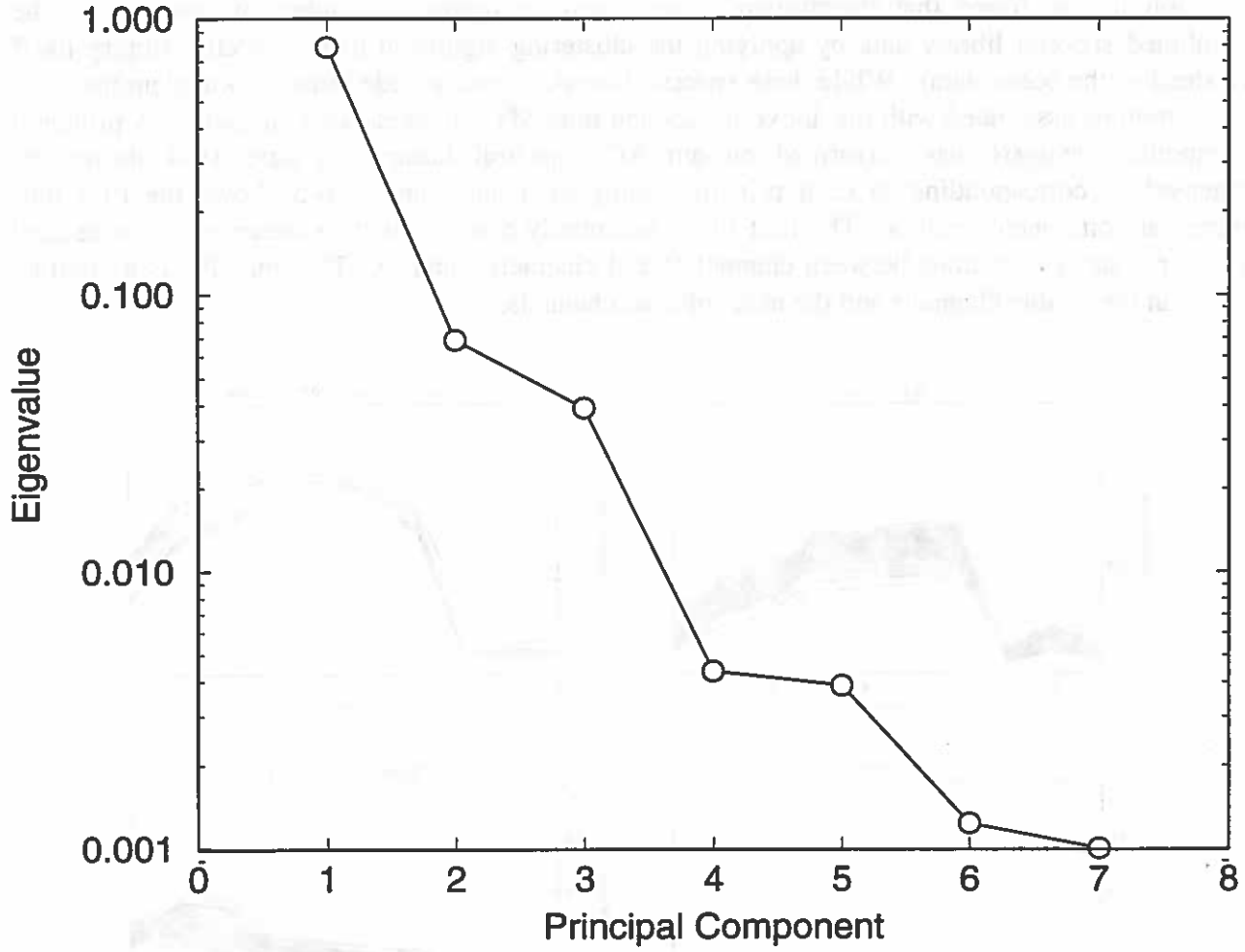

Figure 16-4. Eigenvalues versus principal component for combined spectral libraries.

The first step of the material identification algorithm is to perform a principal component analysis on the MTI scene data. Principal components containing only noise or instrumental effects are removed from the dataset. Next the k-means clustering algorithm is applied to the scene in the principal component domain resulting in N cluster centers, where N is the predetermined number of clusters to be found. The result of this step is a set of N spectral signatures (in the PC domain) corresponding to each of the N clusters. The mean cluster PC spectra are then rotated from the principal component domain back to the spectral domain and compared with the spectral library for the best matches. A label is then applied to each pixel corresponding to its best match in spectral library.

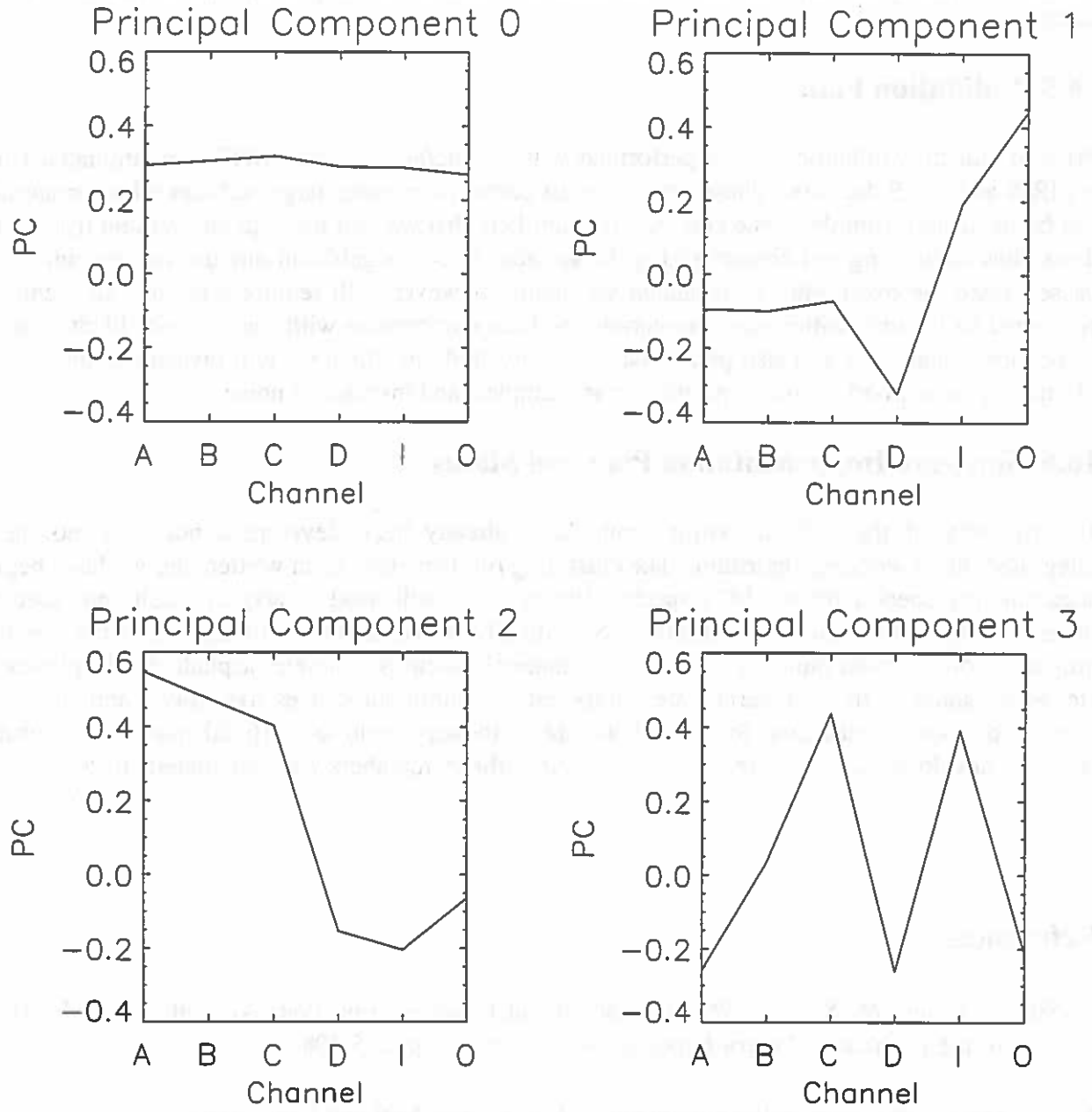

Figure 16-5. First four principal components.

16.4 Error Budget

A potential source of error is improper atmospheric corrections. The atmospheric correction process calculates surface reflectivity from the solar irradiance and the measured reflectance. Aerosol scattering properties are wavelength dependent. Thus if the atmospheric correction algorithm incorrectly estimates the amount of aerosol the resulting surface spectral reflectivity will be in error and may bias the clustering results. It is also very important that the spectral libraries

fed into this algorithm contain the spectral signatures of all potential materials of interest. If a certain material is not represented in the library, it will never be properly identified in a given scene.

16.5 Validation Plan

Prior to launch, validation will be performed with visible/near infrared MTI data simulated from AVIRIS and MAS datasets. These datasets must contain numerous large surfaces whose materials can be identified from the scene context. It is unlikely that we will have quality ground truth from these sites identifying and characterizing the surfaces since a significant amount of time will have passed since the overflight. Post-launch validation, however, will require a number of technical personnel to identify within-scene materials for later comparison with the material identification algorithm output. We will also perform a sensitivity study in which we will investigate the effects of mixed pixels, poorly chosen spectral library samples, and instrument noise.

16.6 Software Implementation Plan and Status

The majority of the software components have already been developed, but have not been integrated into a working algorithm. The clustering routines have been written and we have begun accumulating spectra for the MTI spectral library. We still need to acquire additional spectral libraries relating to man-made materials. Specifically we need more information on the spectral properties of common building construction materials such as concrete, asphalt, brick, plywood, etc. Since some of these materials are composed of natural substances like gravel and sand, we need to pay special attention to these if we are to identify them as artificial materials. Further software development is required to match spectral library members with calculated clusters.

References

Al-Sultan, K. and M. Khan, 1996, "Computational Experience on Four Algorithms for the Hard Clustering Problem," *Pattern Recognition Letters*, **17**, pp. 295-308.

Naivar, Mark, 1997: personal communication, Los Alamos National Laboratory.

Theiler, J., and G. Gisler 1997, "A contiguity-enhanced k-means clustering algorithm for unsupervised multispectral image segmentation," *Proc. SPIE*, **3159**, pp. 108-118.

18. THE MTI MODELING AND ANALYSIS DATABASE: MTIDB

John J. Szymanski and Pierre Villeneuve

18.1 Introduction and Goal

It is important that the modeling and analysis work use a consistent set of parameters for spacecraft attributes, performance parameters, etc. To accomplish this, a database has been created called MTIDB.

In addition these file formats contain the ancillary data that is necessary to process data into higher Levels.

The suffix ".pan" stands for "Parameter Array Input."

18.2 Software Implementation Plan and Status

MTIDB is now functioning with a set of input files and the software to read them into IDL codes. The following files have now been defined and partially filled:

```
alignment.pan       ; Parameters defining the relative alignment of the
                    ; FPA, telescope, and bus.
cal_geom.pan        ; Geometrical and physical parameters of the OBCS.
example.pan         ; Examples of how to format each entry type.
fpa_geom.pan        ; Geometry parameters for the FPA.
gcal0.pan           ; Ground calibration constants.  The 0 is an index
                    ; to keep track of the many ground calibration runs.
mat_props.pan       ; Thermophysical properties of various metals.
obcs%%%%.pan        ; On-board calibration constants.
```

operation%%%%.pan	; Operational parameters defining the image ; acquisition.
orbit%%%%.pan	; Orbital parameters.
payload_geom.pan	; Master list of payload parameters.
performance%%%%.pan	; Sensor performance parameters (SNR, PSF, etc.)
phys_const.pan	; General physical constants.
regis%%%%.pan	; Image registration information.
soh%%%%.pan	; State-of-health parameters.
telescope.pan	; Telescope optics parameters.

The designation %%%% stands for an image number and indicates that the file contains information that may change from one image acquisition to another.

The database allows including other database files, reading of data files whose contents are binary or text, as well as a number of different variable types within the .pan files (including arrays). Two IDL codes have been written to read the database files. A third IDL code reads a database file and produces an IDL include file with a list of variables defined from the database file. Example.pan is the main documentation source for using the database, and the .pan files are designed to have extensive documentation within the variable definitions. The .pan files are located in:

$MTISOFT/Working/data/mtidb

and the database read files are in:

$MTISOFT/Working/pro/mtidb